HIGH FREQUENCY TRANSMIT-RECEIVE PHASED ARRAY COIL FOR HEAD AND NECK MR NEUROIMAGING AT 3 TESLA

By

SHMUEL GOTSHAL

A THESIS PRESENTED TO THE GRADUATE SCHOOL
OF THE UNIVERSITY OF FLORIDA IN PARTIAL FULFILLMENT
OF THE REQUIREMENTS FOR THE DEGREE OF
MASTER OF SCIENCE

UNIVERSITY OF FLORIDA

2003

This work is dedicated to my loving wife Noa and three children, Snir, Yarden and Sa'ar, without whom I would not have had the support I needed to complete this work.

ACKNOWLEDGMENTS

I would like to thank the following individuals for their assistance that made this work possible. The greatest thanks go to my advisor, Dr. Jeffrey R. Fitzsimmons, for taking time out of his busy schedule to review my work, offer advice and support my efforts—with a great patience to my slow progres. Thanks also go to Dr. G. Randy Duensing and Dr. Charley Saylor for stimulating discussions and advice throughout this project. Thanks are also well deserved to Dave Peterson who helped me with the system operation and was willing to be the volunteer in some of the clinical imaging and experiments. I also thank Larry Hyler for his help with picture taking and image formatting.

TABLE OF CONTENTS

LIST OF TABLES

LIST OF FIGURES

Abstract of Thesis Presented to the Graduate School
of the University of Florida in Partial Fulfillment of the
Requirements for the Degree of Master of Science

HIGH FREQUENCY TRANSMIT-RECEIVE PHASED ARRAY COIL
FOR HEAD AND NECK MR NEUROIMAGING AT 3 TESLA

By

Shmuel Gotshal

May 2003

Chair: Jeffery R. Fitzsimmons
Major Department: Biomedical Engineering

A new transmit-receive phased array coil is presented for neurovascular imaging at 3T. A transmit-receive configuration was chosen in order to minimize the required RF power, reduce the deposited average SAR, and avoid the safety issues that are typically related to the use of whole body coils at high frequency. Field simulation of the individual elements of the phased array was performed and specific absorption ratio (SAR) was calculated. A power splitter was designed, optimized and implemented to obtain uniform excitation in the entire volume covered by the coil. B1 maps (as flip angle maps) were reconstructed to show that the target uniformity was achieved. Results are shown on volunteer images in 3 slice orientations. Phantom images and signal-to-noise ratio (SNR) analysis are shown in comparison to a standard 3T head coil (GE Medical Systems). In addition, The high SNR and high-resolution capabilities of the 3T

neurovascular array are demonstrated in clinical imaging of the cervical spine area, as well as in short acquisition time angiography (MRA) studies of the carotids.

CHAPTER 1
MAGNETIC RESONANCE THEORY

Nuclear Magnetic Resonance

Quantum Description

The atomic nucleus possesses a quantum mechanical property known as *spin*, a vector quantity given the symbol **I**. If the spin of a nucleus is non-zero, then it has a total angular momentum $\mathbf{J} = \hbar\mathbf{I}$ and a magnetic moment $\boldsymbol{\mu}$ in parallel. The magnetic moment is given by

$$\mu = \gamma \hbar \mathrm{I}. \qquad [1.1]$$

where $\hbar = h/2\pi$ and h is Planck's constant, and γ is a constant of proportionality—the magnetogyric ratio.

When this nucleus is placed in an external static magnetic field $\mathbf{B_0} = \mathrm{B}_0\ \hat{\mathrm{k}}$, there are several possible energetic levels, known as Zeeman levels. The separation of the different levels is proportional to the magnetic field strength. In the case of a spin ½ nucleus such as ^{1}H, there are two possible energy levels given by

$$\begin{aligned} \mathrm{E}_1 &= -\boldsymbol{\mu} \bullet \mathbf{B_o} = -\gamma \cdot \hbar \cdot \tfrac{1}{2} \cdot \mathbf{B_0} \\ \mathrm{E}_2 &= -\boldsymbol{\mu} \bullet \mathbf{B_o} = \gamma \cdot \hbar \cdot \tfrac{1}{2} \cdot \mathbf{B_0} \end{aligned} \qquad [1.2]$$

Transitions between spin states are allowed only for a change in energy equal to the difference between the two levels as follows:

$$\Delta \mathrm{E} = \mathrm{E}_1 - \mathrm{E}_2 = \gamma\hbar \mathrm{B}_0 \qquad [1.3]$$

For this transition to occur (1), the spin system must obtain RF energy from a time varying magnetic field (**B_1**) directed perpendicular to the static field and oscillating at a frequency (ω_0), where

$$\Delta E = h \cdot \upsilon \qquad [1.4]$$

From Eq. [1.3] and [1.4] the Larmor frequency is found:

$$\begin{aligned} &2\pi \cdot \hbar \cdot \frac{\omega_0}{2\pi} = \gamma \hbar B_0 \\ &\Rightarrow \omega_0 = \gamma \cdot B_0 \end{aligned} \qquad [1.5]$$

This Larmor equation describes what is referred to as the nuclear magnetic resonance condition.

Classical Description

In the classical description, a particle possessing a magnetic moment placed in a magnetic field will experience a torque. This torque will cause a precession of the magnetic moment about the field (for example, a spinning top under the influence of gravity). This is shown in Fig. 1.1a for a single nucleus of magnetic moment, μ.

However, real life macroscopic samples require an ensemble picture that describes populations of spins in specific spin states. In the case of a macroscopic sample of spin ½ nuclei in a static magnetic field, the two possible spin states or populations are spins aligned with the **B_0** field (N_+) and spins anti-aligned with the **B_0** field (N_-). The distribution of spins in these states is governed by the Boltzmann distribution that depends on the energy difference between states, the temperature (T) of the surrounding environment and the Boltzmann constant *k*, such that,

$$\frac{N_+}{N_-} = \exp\left(\frac{\Delta E}{kT}\right) \approx 1 + \frac{2\mu B_0}{kT} \;\; for\, \Delta E << kT\,. \qquad [1.6]$$

Therefore, there is a small, net magnetization, $M = \sum_{i=1}^{N} \mu_i$, parallel to $\mathbf{B_0}$ (Fig. 1.1b).

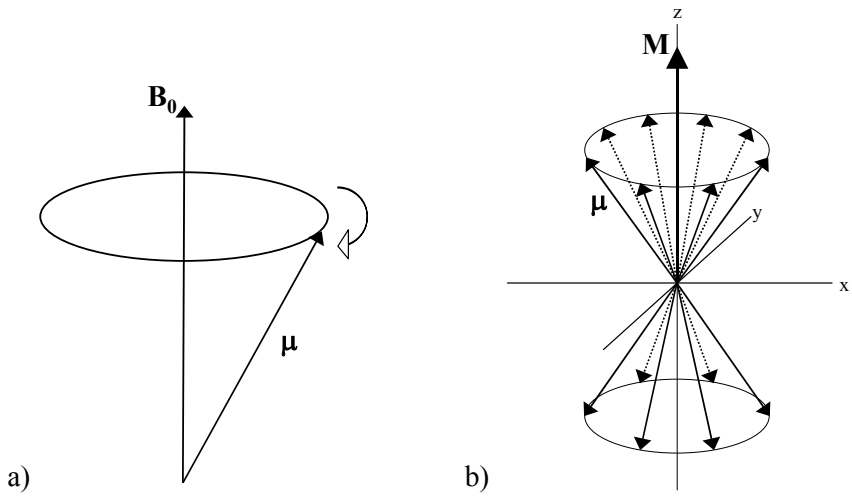

Figure 1.1. Precession of a magnetic moment **μ** about a magnetic field B_0. a) For a single spin. b) For an ensemble of spin magnetic moments, giving rise to a net magnetic moment **M**.

The equilibrium magnitude of this magnetization (M_0) is proportionally related to B_0 and is given by

$$M_0 = \frac{\gamma^2 \hbar^2 B_0 N_0}{3kT} I(I+1) = \chi B_0 , \qquad [1.7]$$

where N_0 is the number of nuclei per 1 m^3 of the sample. The sample magnetic susceptibility, χ, is a constant dependent on the temperature and composition of the sample.

For the net magnetization vector M of a sample placed in a magnetic field **B** the equation of motion is given by

$$\frac{d}{dt}\mathbf{M} = \gamma \mathbf{M} \times \mathbf{B} . \qquad [1.8]$$

In order to achieve NMR excitation, an external oscillating magnetic field is applied orthogonal (or transverse) to the static magnetic field. In general, such a magnetic

field ($\mathbf{B_1}$) is circularly-polarized field in the transverse (x-y) plane, and oscillating at the Larmor frequency (ω_0).

Therefore, the effective B_1 field can be written as

$$\mathbf{B}_1(t) = B_1[\mathbf{i}\cos(\omega t) - \mathbf{j}\sin(\omega t)]. \qquad [1.9]$$

Applying the RF B_1 field to the magnetization in the static B_0 field, the equation of motion becomes

$$\frac{d}{dt}\mathbf{M} = \gamma\mathbf{M}\times[\mathbf{B}_0 + \mathbf{B}_1(t)] = \gamma\mathbf{M}\times\mathbf{B}_{eff}. \qquad [1.10]$$

Relaxation

Spin-lattice (T1) relaxation

At equilibrium, the net magnetization vector lies along the direction of the applied magnetic field $\mathbf{B_0}$ and is called the equilibrium magnetization $\mathbf{M_0}$. In this configuration, the Z component of magnetization $\mathbf{M_z}$ equals $\mathbf{M_0}$. $\mathbf{M_z}$ is referred to as the longitudinal magnetization as shown in Fig. 1.2. There is no transverse ($\mathbf{M_x}$ or $\mathbf{M_y}$) magnetization yet.

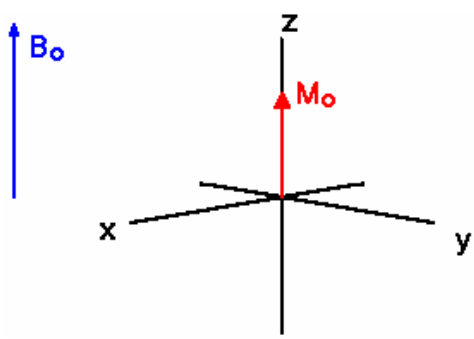

Figure 1.2. At equilibrium, M is aligned with B_0.

It is possible to change the net magnetization by exposing the nuclear spin system to energy of a frequency equal to the energy difference between the spin states (RF pulse). If enough energy is put into the system, it is possible to excite the spin system, so that **M** is at the transverse plane (X-Y plane) and $\mathbf{M_Z}$=0.

If the excitation pulse were then stopped, the magnetization vector would return to its equilibrium value with relaxation time constant called the spin lattice relaxation time (T_1). This relaxation releases energy in the Larmor frequency as a signal known as free induction decay (FID). This signal can be detected by a special antenna (RF coil), positioned perpendicularly to M_0, to collect the data for image reconstruction.

This process is described by

$$\frac{d}{dt}M_z = -\frac{(M_z - M_0)}{T_1}, \qquad [1.11]$$

where T_1 is the longitudinal relaxation time.

Spin-spin (T2) relaxation

When the net magnetization is displaced towards the XY plane using RF pulse, it will rotate about the Z-axis at a frequency equal to the Larmor frequency (Fig.1.3 a). In addition to the rotation, the net magnetization starts to dephase because each of the spin packets making it up is experiencing a slightly different magnetic field and rotates at its own Larmor frequency. The longer the elapsed time, the greater the phase difference which causes a decay of the transverse magnetization $\mathbf{M_{xy}}$ (Fig 1.3 b). The time constant, which describes the return to equilibrium of the transverse magnetization, $\mathbf{M_{xy}}$, is called the spin-spin relaxation time, T_2.

This relaxation effect on the transverse components of magnetization is described by

$$\frac{d}{dt}M_{x,y} = -\frac{M_{x,y}}{T_2}, \qquad [1.12]$$

where T_2 is known as the transverse relaxation time.

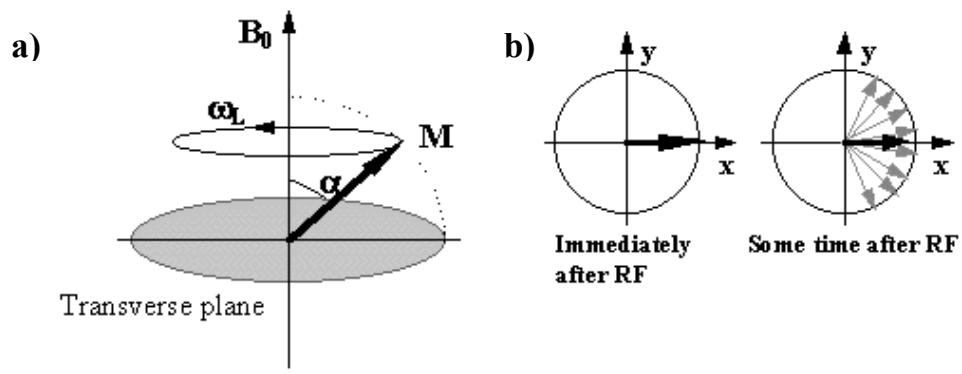

Figure 1.3. Dephasing of spin components causing T_2-relaxation and hence a reduced transverse magnetization ($\mathbf{M}_{xy}$).

The observed transverse relaxation time is shortened if $\mathbf{B_0}$ inhomogeneities are present within the sample. Much like T_2 relaxation, the variation in the local $\mathbf{B_0}$ field causes variation in the precessional frequency of the isochromats, in this case, depending on their position within the sample. Therefore, the effective transverse relaxation time (composed of both T_2 relaxation and the effects of $\mathbf{B_0}$ inhomogeneity) is labeled T_2*, such that $T_2^* \leq T_2$. The decay of the transverse magnetization is also exploited in several ways for both MR imaging and spectroscopy.

Bloch Equations

Combining the relaxation term into the motion equation [1.10] yields a set of differential equations, known as the Bloch equations (2), describing the magnetization under influence of a static $\mathbf{B_0}$ field, a time dependent RF $\mathbf{B_1}$ field and relaxation effects (3) as follows:

$$\frac{d}{dt}M_x = \gamma[M_y B_0 + M_z B_1 \sin(\omega t)] - \frac{M_x}{T_2},$$
$$\frac{d}{dt}M_y = \gamma[-M_x B_0 + M_z B_1 \cos(\omega t)] - \frac{M_y}{T_2}, \qquad [1.13]$$
$$\frac{d}{dt}M_z = \gamma[-M_y B_1 \cos(\omega t) - M_x B_1 \sin(\omega t)] - \frac{(M_z - M_0)}{T_1}.$$

The magnetization response to any RF pulse sequences can be described by numerically solving the Bloch equations.

Excitation and Flip Angle

With the initial magnetization parallel to $\mathbf{B_0}$ (+z-direction), if the $\mathbf{B_1}$-field is applied along the +x-axis with the Larmor frequency for a time τ, the magnetization vector rotates by an angle θ, given by

$$\theta(t) = \gamma \int_0^{\tau} \mathbf{B_1}(t)dt \qquad [1.14]$$

The angle θ is called the flip angle. As will be discussed later, flip angles of 90° (magnetization lies in the transverse plane) and 180° are of special interest in NMR.

Magnetic Resonance Imaging

Spin Echo

A spin echo, first proposed by Hahn in 1950 (4), occurs when two excitation pulses are applied in the following sequence: 90° - τ - 180°, where τ is a time interval between the pulses. The solution of the Bloch equations for $t = 2\tau$ is then given by

$$M_x = 0$$
$$M_y = -M_0 \cdot e^{-\frac{2\tau}{T_2}} \qquad [1.15]$$
$$M_z = M_0 \cdot \left[1 - e^{-\frac{\tau}{T_1}}\right]^2$$

The meaning is that at time $t = 2\tau$ the magnetization is not dependent on ω (the local resonance frequency that a spin experiences). Therefore, all elements of the magnetization have refocused along the +y-direction to create the echo, as in Fig. 1.4.

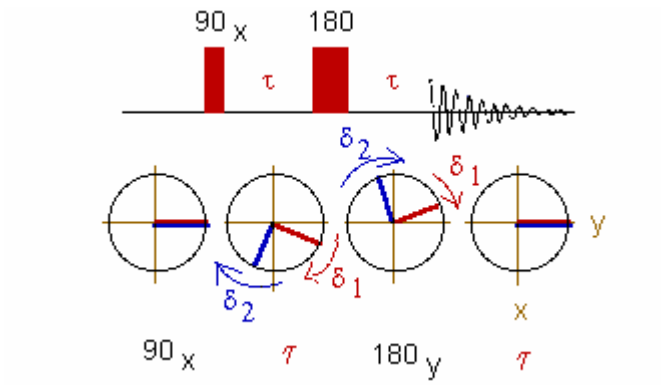

Figure 1.4. The formation of a spin echo.

Magnetic Field Gradient

If each of the regions of spin were to experience a unique magnetic field we would be able to image their positions. A gradient in the magnetic field is what will allow us to accomplish this. A magnetic field gradient is a variation in the magnetic field with respect to position. A one-dimensional magnetic field gradient is a variation with respect to one direction, while a two-dimensional gradient is a variation with respect to two. The most useful type of gradient in MRI is a one-dimensional linear magnetic field gradient along each one of the principle axes x, y and z, such that the total magnetic field is

$$\mathbf{B}_{\mathbf{tot}} = \mathbf{B}_{\mathbf{0}} + \mathbf{G} \bullet \mathbf{R} \qquad [1.15]$$

where $\mathbf{G} = G_x\hat{i} + G_y\hat{j} + G_z\hat{k}$ is the gradient vector, and **R** is the spatial vector.

The Larmor frequency at each point is then given by

$$\omega(x, y, z, t) = \gamma \cdot \mathbf{B}_{\mathbf{tot}} = \gamma\mathbf{B}_{\mathbf{0}} + \gamma \cdot \mathbf{G} \bullet \mathbf{R} \qquad [1.16]$$

This allows to perform thin slice excitation (slice selection), as well as two-dimensional encoding necessary for image reconstruction.

Slice selection

Eq. [1.16] can be written as

$$\frac{\omega}{\gamma} = \mathbf{B_0} + G_x x + G_y y + G_z z \qquad [1.17]$$

which implies that the excitation frequency ω and the gradients may be used to determine a plane, in which the excitation frequency equals to the Larmor frequency. Only spins in this plane would experience the nuclear magnetic resonance condition, and therefore will be flipped to the transverse plane.

From practical reasons, and in order to obtain excitation in a slice of finite width, a pulse with finite bandwidth (Δω) is required. It is possible to achieve such a pulse with a rectangular frequency profile by using a sinc (sin(ωt)/ωt) shaped RF pulse. However, a perfect rectangular-shape slice profile would require an infinitely long RF pulse. For a practical finite length RF pulse, the edge of the profile becomes less defined and side lobe(s) appear on each side. This effect can be cut down using a several filtering techniques, which shape the RF pulse in order to optimize the slice profile (5).

Frequency encoding

After slice is selected and excited, two-dimensional spatial information over the slice is required. One of these dimensions is encoded using the frequency encoding method:

At isocenter, the magnetic field is B_0 and the resonant frequency is ω_0. If a linear magnetic field gradient is applied, each region experiences different magnetic fields. The result is a NMR signal with a non-zero frequency bandwidth. The amplitude of each

frequency component in the signal is proportional to the number of spins in the location associated with this frequency. This procedure is called frequency encoding and causes the resonance frequency to be proportional to the position of the spin.

Assuming that the frequency encoding gradient (also called read gradient) is applied in the x-direction, the difference in resonance frequency at each location versus the isocenter is given by

$$\Delta\omega = \gamma \cdot G_x \cdot x \qquad [1.18]$$

Phase encoding

Similar to the description of the frequency encoding, if a gradient in the magnetic field is applied along the y-direction, each spin location along this axis would experience different resonance frequency. However, this property alone can not be used again, since we already encoded by frequency in the x-direction. Nevertheless, it is important to notice that if this gradient is applied for a fixed time and then stopped, the precessed spins acquire phase differences based on their position along the y-axis. This phase difference is maintained even after the gradient operation is stopped.

For a gradient applied in the y-direction for a period t the total spin phase is

$$\varphi(y) = \gamma \cdot G_y \cdot t \cdot y \qquad [1.19]$$

If the gradient in the y-direction is turned off, the external magnetic field experienced by each spin location is, for all practical purposes, identical. Therefore the Larmor frequency of each transverse magnetization vector is identical. However, the phase difference that was created during the operation of the gradient is preserved, and the spins will continue to precess with this phase difference.

FT Tomographic Imaging

In typical MRI procedure, one axis gradient is used for slice selection, while the other two are used for 2D encoding (frequency and phase) of the selected slice. It can be shown that the acquired data collected during the MRI process is the 2D Fourier Transform of the slice image. Therefore the acquired data is to be Fourier Transformed to obtain the required image. This is illustrated in the Fig 1.5 for the imaging of two voxels with net magnetization in the imaged plane.

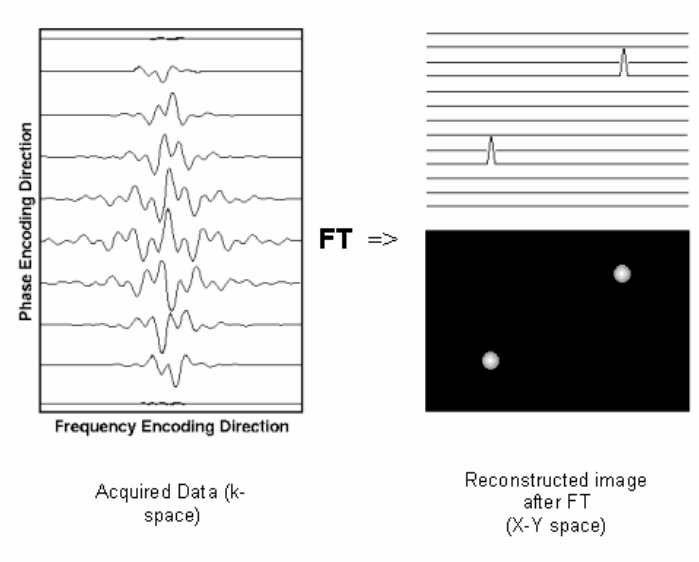

Figure 1.5. Fourier image reconstruction.

CHAPTER 2
BACKGROUND OBJECTIVES AND HYPOTHESIS

Background

Phased arrays that were first introduced in 1990 (6) are widely used in magnetic resonance imaging (MRI). A phased array is a plurality of closely positioned RF coils, which cover the required field of view (FOV). Each element is then connected to a preamplifier and a separate receiver channel, where the signals are digitized and combined. This way a high signal-to-noise ratio (SNR)—associated with relatively small coil elements – is obtained over the extended field of view. In addition to the extended FOV, phased arrays enable to receive signal from a given voxel, using more than one coil element. Provided that the multiple coil elements can be isolated from each other, this may improve the image SNR by the square root of the number of elements.

Since the early 1990's phased array coils have been used in a variety of configurations, covering the desired field of view by planar (surface), volume, or combined elements arrangement. Nowadays, most clinical MRI systems offer multi-channel receivers, with typically four receiver channels. Eight channel systems are also available, and probably will become the industry standard in the near future. Multiple coil arrays have many advantages, even beyond SNR and image quality. Recent imaging techniques such as SENSE and SMASH (7,8) allow significant scan time reduction using spatial encoding information of the phased array coil.

In recent years there has been an increase in usage of MRI systems at field strength above the typical 1.5 Tesla. Research systems have been built with magnets as high as

14T. Moreover, clinical systems are now commercially available at 3T and 4T. Yet, these systems are mainly used for research and clinical applications in functional MRI (fMRI), and other head related studies. Whole body applications are very limited, mainly due to the fact that these commercial systems currently do not have whole body RF coils.

The principle advantage of MRI at 3T compared to the more commonly used systems of 1.5T, are that inherent SNR and chemical shift are higher, as well as that spin-lattice relaxation time constant (T1) is increased (9). These advantages can provide significant improvement in image quality and resolution not only in head imaging, but also in other high-resolution applications such as cardiac imaging, spine and vascular studies.

Therefore, whole body RF coils at 3T have recently been developed (10,11), in order to use in conjunction with a variety of receive only coils and phased arrays. However, whole body RF coil design at high field (3T and above) are subject to a series of potential obstacles and problems, mainly but not solely, related to the required RF power and patient safety:

- It is well known in MRI system design, that RF power required to produce the RF magnetic field (B_1) is increased approximately as a linear function of the static field (B_0) strength. Therefore, a 3T whole body coil would generally require four times higher RF power than a typical 1.5T body coil. As these types of high frequency, high power RF amplifiers are not only very expensive, but also not commonly available, this present a major constraint in using a large and less efficient RF coil such as a whole body coil.

- The sample-induced voltage is linearly proportional to frequency, so that the power deposited into the sample is 4 times higher in 3T system than in 1.5T (9). This problem is enhanced with a whole body RF coil since the sample volume, which is exposed to RF transmission, is generally larger.
  The amount of RF power deposited in a sample unit of mass is defined as SAR (specific absorption ratio, measured in w/kg units). Maximum allowed SAR levels (average and local) are determined by FDA guidelines and are closely monitored in MRI systems.

- Several imaging techniques, which are based on frequency definition of different materials (e.g. chemical suppression), would be optimized if RF excitation is perform only within the region of interest.

Significance and Objectives

Significance

The design of a Neurovascular phased array coil for 3T addresses the need for more SNR capability in a large field of view in the head and neck region. In addition, as many of the imaging techniques in these areas require fast imaging and short acquisition time, the inherent high SNR of this coil allows effective reduction of scan time, which also minimizes undesired artifacts.

As MRI systems development is focused towards higher field magnets, power requirement considerations are of concern. The power required to produce a 90 degree pulse is approximately linear function of field strength, so that at 3T system the available power needs to be four times higher than the power required at 1.5T. One possible solution to this problem is by modifying the RF transmit pulse so that it is longer in time, and therefore lower peak value of the magnetic field is needed. Actually, this method can be very effective in reducing the RF power. For example, if the pulse width (in time) is reduced by a factor of 2, only half the peak value is required to obtain the same flip angle, and hence the pulse peak power is reduced by a factor of 4. However, accuracy of the excited slice profile (that is associated with the transmit pulse) would require narrow RF pulses, so that the above method leads to compromised image quality.

The Neurovascular array presented in this work addresses this problem by excitation of much smaller volume – only this required for the imaging. The local nature of transmitting with this coil requires much lower power than a whole body coil. The

estimated power is in the order of 2-3kw, in compare to approximately 25kw (11) that would be necessary with a whole body RF coil.

This lower required power is not only an economic advantage, it is also important for patient safety. As a result of the power absorbing properties of biological tissue at high frequencies, RF power required to drive whole body coil may be limited by the FDA regulations regarding specific absorption rate (SAR). The use of local coil for transmit reduces the average SAR level. In addition the lower RF voltage and current that is required to drive a smaller coil, can reduce patient heating related to E-field effects close to the coil conductors. This allows more flexibility in prescribing the protocols, as more slices and higher repetition rate can be employed.

Other advantages of the Transmit/Receive Neurovascular Array over the use of a whole body transmit coil and a local receive-only array, are related to imaging techniques and image artifacts. One of the artifacts in imaging with a receive only coil, arises from the fact that the whole body coil excites not only the tissue in the imaging area, but also outside this region. This fact, together with selecting a field of view that is larger than the imaged object, causes the problem known as wrap around, where signal from outside the field of view is folded into the image. A typical solution to the problem in single dimension is by selecting the phase encoding direction properly. This creates an undesired constrain in scan parameter selection. However, the use of smaller transmit coil which does not excite tissue outside the interesting field of view eliminates the artifact completely.

Other applications that would prefer local tissue excitation are spectroscopy, magnetization transfer methods (12) and chemical suppression. These methods are based

on the different resonance frequency of different materials (for example water and fat). In order to utilize these methods in the head and neck region, a transmit-receive coil is preferred.

Objectives

Aim 1—field distribution

The field distribution of the Neurovascular array was modeled and analyzed at high frequency (127.75MHz). This includes characterization of RF field patterns, field-tissue interaction and RF field uniformity. Based on the field analysis, the optimal coil geometry and number of elements were determined.

Aim 2—electric properties

The electrical properties of the Neurovascular array were analyzed at high frequency (127.75MHz). This includes investigation of coil self inductance, coil losses (resistance) and mutual inductance between the array elements. In addition, cross-talk and noise correlation between the coil elements were investigated, and methods for mutual inductance cancellation were used

Aim 3—volume transmit/receive array

A volume transmit/receive Neurovascular array was developed for the application of Head & Neck MR Neuroimaging at 3.0 Tesla. This array was based on a four-channel receiver hardware and the actual design was based on the simulation in Aim 1. The design goals were:

- Signal-to-Noise Ratio (SNR)—the new coil performance and image quality (SNR) is expected to be at least similar to those of the existing head coil (16 rungs Birdcage) with additional coverage in the neck area.
- Homogeneity—the field profile and the image intensity were required to be uniform within ±20% in a sphere of 20cm diameter around the head coil center. Penetration in

the neck area will provide good imaging quality of the cervical spine and carotid arteries.

- Impedance matching and Isolation—the coil elements need to be matched to 50Ω, and the isolation between the elements in the array should be better than -15dB.
- SAR—the average and local SAR levels are required to be within the FDA guidelines for head and neck imaging.

Aim 4—transmit circuits

Transmit circuits—power splitter, T/R switches and phase shifters—were designed to feed the phased array in the transmission mode. Coil coupling during transmission was analyzed and compensated by varying the amplitude and relative phases, such that the transmit field uniformity is better than ±15% in the head and neck region.

Aim 5—specific absorption ratio (SAR)

Average and local SAR levels were estimated by simulation, to ensure that coil operation is within the FDA guidelines.

Aim 6—clinical imaging

The Neurovascular array was tested on human volunteers to provide clinical data of the brain, cervical spine and head and neck vascular system. In particular importance, the vascular structures of the carotid arteries and the circle of Willis were imaged.

Hypothesis

I hypothesize that a robust transmit-receive phased array, that will generate high quality neuroimaging of the head and neck—as specified in Aim 3—can be developed to operate in a 3.0 Tesla MRI system. I further hypothesize that a transmit circuit can be developed, in conjunction with the Neurovascular array, to provide uniform spin excitation in the head and neck regions—as specified in Aim 4.

CHAPTER 3
THE NEUROVASCULAR ARRAY – THEORY AND DESIGN

Theory

B_1 Field Calculation

For a coil used as both transmitter and receiver, the B_1 field amplitude affects both the flip angle of the NMR excitation as well as the reception sensitivity. For a Spin Echo (SE) sequence (4), the signal distribution, *S(r)*, is given by

$$S(\mathbf{r}) \propto \frac{|\mathbf{B_1}(\mathbf{r})|}{I} \sin^3 \theta(\mathbf{r}) \ , \qquad [3.1]$$

where θ(r) is the flip angles experienced at a spin location **r**, and $\frac{|\mathbf{B_1}(\mathbf{r})|}{I}$ is the receiver-coil sensitivity (13), where $\mathbf{B_1}(\mathbf{r})$ is the field produced by a current I ($\hat{\mathbf{B}}_1(\mathbf{r})$ for unit current).

This field can be modeled and analyzed using the quazi-static approximation, in which the field $\mathbf{B_1}(\mathbf{r})$ produced at any point **r**, by an arbitrary current I located at any point **r'**, is given by Biot-Savart law (14) as follows:

$$\mathbf{B_1}(\mathbf{r}) = \frac{\mu_0}{4\pi} \cdot \int_L \frac{\mathbf{dI} \times (\mathbf{r} - \mathbf{r'})}{(\mathbf{r} - \mathbf{r'})^3} \qquad [3.2]$$

where μ_0 is the magnetic permeability of free space, **dI** is the element current vector at location **r'** and L is the path of wire carrying the current **I.**

This magnetic field calculation represents the unloaded field of the coil or the coil sensitivity. It is also a measure for the NMR signal sensed by the coil. In order to

evaluate the loading effect, and the loaded performance of the coil, the RF power absorbed by the sample need to be calculated.

Noise and Power Deposition

Neglecting radiation resistance and noise from the receiver electronics, the noise voltage picked up by the receiver is proportional to the square root of the sum of the effective resistance of the sample (R_S) and the resistance of the coil itself (R_C) (13). At high frequency, and under loaded condition, the coil self-resistance may be neglected, so that noise is contributed only from the sample resistance. Furthermore, dielectric loss within the sample (15) can be effectively minimized by using distributed capacitance and balanced matching circuits (16,17), therefore, only inductive losses associated with RF induced eddy currents, the major source of power deposition within the sample, will be considered (15).

In the quasi-static approximation, the total power deposition (P) or total SAR is calculated from the induced current density which is proportional to the electric field, **E**, in the sample of constant conductivity σ, so that

$$\mathrm{P} = \int_{\text{sample}} \mathrm{P}(\mathbf{r})\mathrm{dV} = \frac{\sigma}{2} \cdot \int_{\text{sample}} \left|\mathrm{E}(\mathbf{r})\right|^2 \mathrm{dV} \qquad [3.3]$$

where P(**r**) is the power distribution in the sample volume V, and σ is the sample conductivity.

The induced electric field E in the sample is calculated from the vector potential A and by Faraday's law (14) as follows:

$$\mathrm{E}(\mathbf{r}) = -\frac{\mathrm{dA}}{\mathrm{dt}} = -\frac{\omega \cdot \mu_0}{4\pi} \int_{\mathrm{L}} \frac{\mathbf{dI}}{(\mathbf{r} - \mathbf{r}')} \qquad [3.4]$$

where ω is the frequency and the integration is along the current path L.

Then, neglecting the power losses in the coil conductors, the Signal to Noise Ratio (SNR) at each location within the volume V is given by

$$\mathrm{SNR}(\mathbf{r}) = \frac{|\mathbf{B}_t(\mathbf{r})|}{\sqrt{P}} \qquad [3.5]$$

Matlab subroutine (`bio_savart_2d_e_3d.m`) (MathWorks, USA) that computes the magnetic field distribution – $\mathbf{B_1}(\mathbf{r})$, and the electric field distribution – $\mathbf{E}(\mathbf{r})$, for any arbitrary current $\mathbf{I}(\mathbf{r})$ is attached in Appendix A.

Bird-Cage Coil Theory

A perfectly homogenous transverse magnetic field in an infinitely long cylinder can be produces by a surface current which runs along the length of the cylinder and has a spatial distribution proportional to sinθ, where θ is the cylindrical coordinate azimuthal angle (18). A good approximation to the ideal current distribution can be obtained by N equally spaced straight wires, each of which includes a capacitor C. The capacitance, together with the self and mutual inductance of the wire structure, creates a circuit which is equivalent to a lumped-element transmission line, as shown in Figure 3.1., where Lr and Lb are the self inductances of the ring elements and bar elements accordingly.

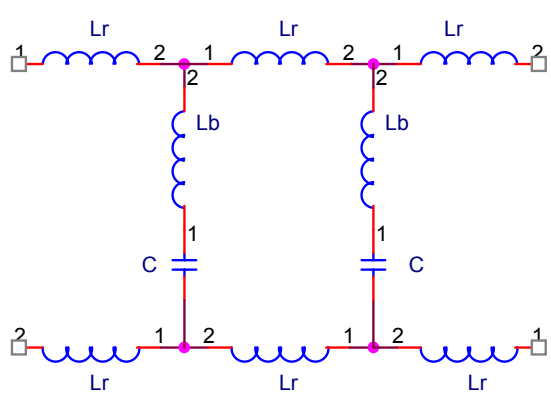

Figure 3.1. A lumped-element equivalent circuit of a Birdcage coil.

If the end points of the circuit are then connected to the start points, such that a closed loop is created, the structure can support only periodical current modes.

Solving the circuit equations of the system in Figure 3.1 (19), yields the resonance frequencies and their associated eigenfunctions, which represent the current distribution for each resonance mode. For the low-pass Birdcage (capacitors on the longitual elements only) the resonance frequencies are given by

$$f_n = \frac{1}{2\pi}\sqrt{\frac{2(1-\cos n\theta)}{C\left[L_r + 2(1-\cos n\theta)L_b\right]}} \qquad [3.6]$$

where θ is the angular separation between bars (2π/N), and n is the mode number. The sinusoidal distribution that is required for uniform transverse field is a special case of the above for n=1. It should also be noted that for this mode the current in the bar segment located at θ=90° is always zero, so that a perpendicular mode, isolated from the first one (fed at θ=0°) can be fed, to obtain a circularly polarized field.

Methods

The 3.0T Neurovascular Array consists of four coil elements as follows:

- A12-bars quadrature Birdcage coil that is used for transmit and reception in the head area. In receive mode the two orthogonal modes of the Birdcage were connected to two receiver channels.
- A transmit-receive Helmholz-Pair (saddle) element (20), that covers the neck region.
- A receive only butterfly elements in the neck area, to enhance SNR in this area.

The configuration of the coil elements in the transmit-receive neurovascular array is shown in Figure 3.2.

The coil was constructed on a Neurovascular coil former (MRI Devices Corp., USA) using both copper tapes and flexible printed circuit boards (PCB). A picture of the coil is shown in Figure 3.3.

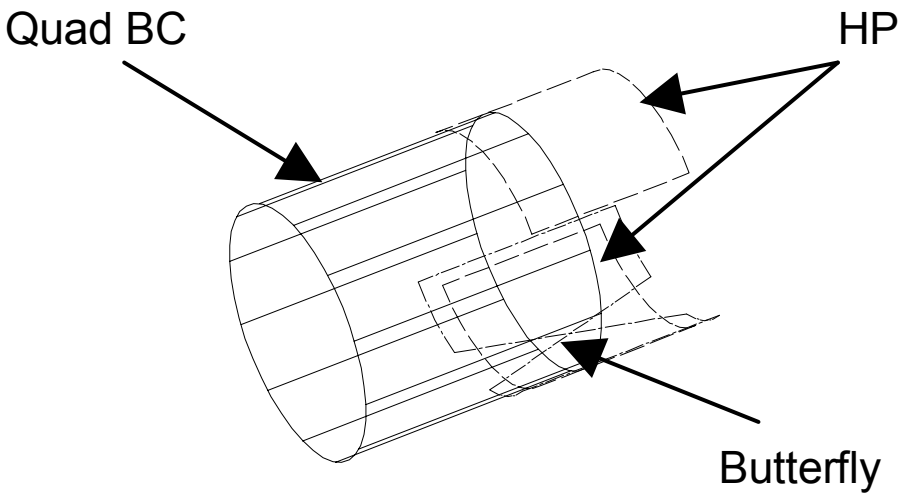

Figure 3.2. The Neurovascular coil configuration.

Figure 3.3. The 3.0T Neurovascular array.

Head Transmit-Receive Coil

Coil design

The Head coil in the Neurovascular Array is a low-pass, 12-bars quadrature Birdcage. The coil inner diameter is 28cm and it is 27cm long.

First, the coil was calculated using the Birdcage Builder program (21) to obtain the required capacitance needed to resonate the coil at the 3.0T frequency (127.75MHz). Results are shown in Figure 3.4.

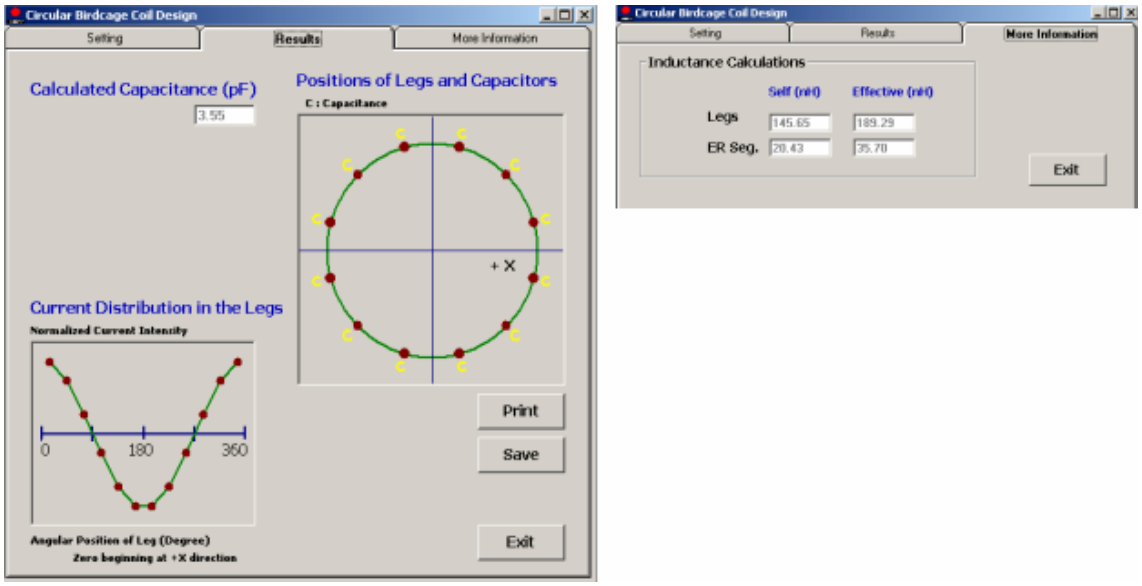

Figure 3.4. Results of the self inductance and the required capacitance as calculated by Birdcage Builder.

The coil was constructed of copper tapes with high voltage capacitors (American Technical Ceramics – ATC, USA). The schematic diagram of the coil is shown below.

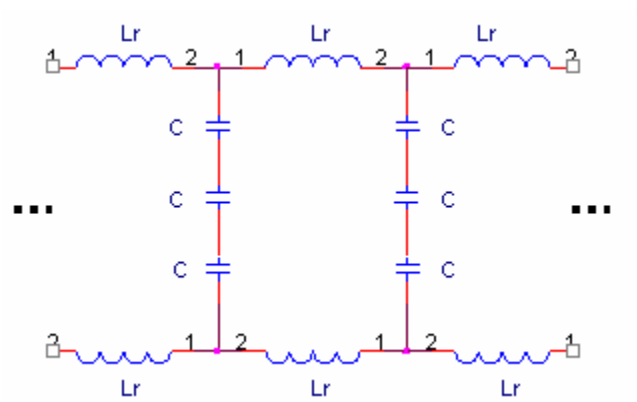

Figure 3.5. Schematic Diagram of the Head Birdcage.

The capacitor C is 10pF, so that the total capacitance in each bar is 3.33pF. For fine-tuning, the capacitance at the main bars (0° and 90°) was adjusted. In addition,

capacitance at the 30° and 60° was adjusted to obtain isolation between the orthogonal modes. The coil input ports were connected to the feed cables through a balanced match circuit (16,17) as shown in Figure 3.6. This circuit provides a balance to unbalance transformation (balun) as well as matching of the input impedance to 50Ω.

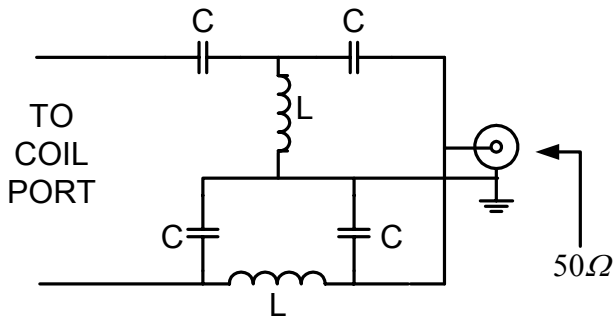

Figure 3.6. Schematic diagram of balance input match.

The simulation model

The model that was used for the quasi-static field simulation is shown in Figure 3.7.

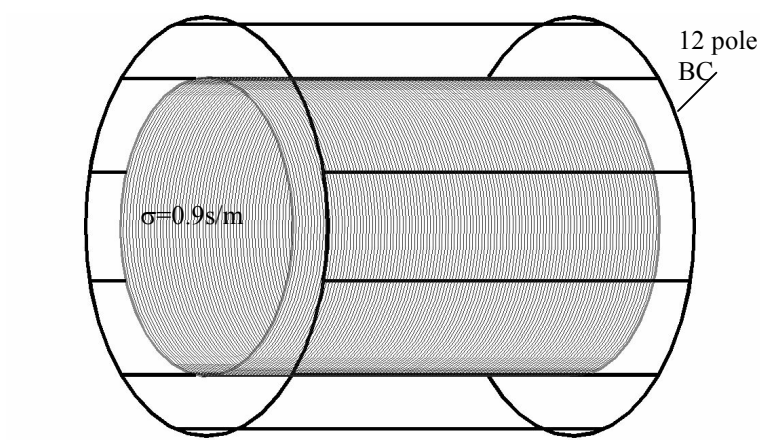

Figure 3.7. The simulation model for the Birdcage coil.

The central cylinder of diameter 20cm and length 27cm represents the sample, with conductivity of 0.9s/m (22). The current conductors are arranged in a Birdcage configuration with diameter of 28cm and length of 27cm. Currents in the Birdcage

longitual segments are according to the sin(θ) distribution, and the end-ring currents are determined by the Kirchoff current law. The resolution of the model, for both current segments and the sample volume is 1 cm in all axes. For distances greater than 1cm from conductors, this resolution was found to be within 5% accuracy when compared to a similar model with 1mm resolution. However, computation time and data storage requirements are significantly lower.

Neck Transmit-Receive Coil

The Neck transmit-receive coil in the Neurovascular array is a Helmholz-Pair (20) coil with length of 20cm and equivalent diameter of 27cm. This coil was isolated from the Birdcage coil by overlap of approximately 3cm. The Helmholtz-Pair configuration was selected for its relative uniform results with minimum number of conductors, which is required due to the open structure of this area in the coil. The structure of the Helmholtz-Pair coil is shown in Figure 3.8.

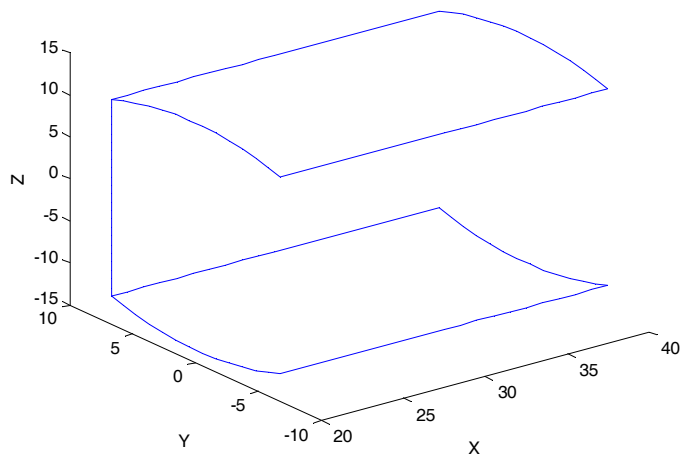

Figure 3.8. The Helmholz-Pair neck coil.

The vertical conductor connecting the two parts is constructed of two coaxial cables to ensure balanced feed and to eliminate any field inhomogenity due to unshielded currents. The two parts of the coil are fed in parallel such that equal current distribution between the two parts is obtained. This ensures optimal A-P field uniformity. In addition, balanced feed, as described before, was used.

Field simulation for the Helmholtz-Pair coil was performed using a similar model as described for the head Birdcage coil, with the Birdcage conductors replaced by the conductor's configuration of Figure 3.8.

Neck Receive-only Coil

The neck receive-only coil in the Neurovascular array is a butterfly shaped coil with length of 20cm. This coil provides a horizontal magnetic field, therefore it is intrinsically isolated from the Helmholtz-Pair coil. Isolation with the horizontal coil in the head Birdcage was obtained by overlap of approximately 3 cm. The butterfly coil was not used for transmission since, as a surface coil, the field is not uniform as penetrating into the sample. This is shown in the following field graph.

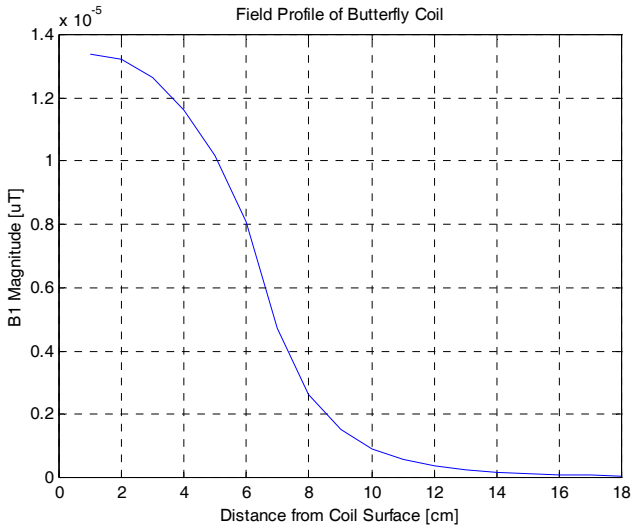

Figure 3.9. Field profile of a butterfly coil.

Using the butterfly coil for transmission would cause a very non-uniform excitation, resulting in either under-tipping the area of interest inside the sample, or over-tipping of the area close to the coil surface. In both cases the result is a nonuniform image. Therefore, trap circuits are used in the butterfly coil in order to decouple it from the transmit elements during the transmission phase. Such a tank circuit is shown in Figure 3.10, where the diodes may be either active PIN diodes (fired by DC current provided by the system), or passive diodes (fired by the RF induced voltage). When the diode is fired, it presents RF short, so that the tune pair—capacitor C and inductor L—is in parallel resonance and creating high impedance in the coil. In the Butterfly coil, an active trap is used at the coil input (with 9415 PIN diode, Microsemi USA) as well as passive traps (with two back-to-back 9701 PIN diodes, Microsemi, USA).

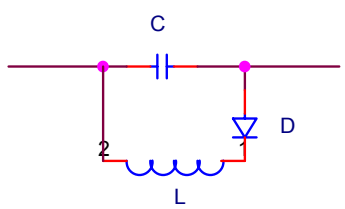

Figure 3.10. A trap circuit in the butterfly coil.

Results and Discussion

Coil Designs

Each coil element was tuned and matched at 127.75MHz, to operate in the GE Signa 3T MR system. The isolation between the coil elements was minimized by adjusting the overlap between adjacent elements. S-parameters result are shown in Table 3.1, where S_{ii} is the insertion loss for the i'th element, and S_{ij} is the isolation between elements i and j.

It should be noted that for elements with the same field orientation, overlapping may cancel the mutual inductance only. However, mutual resistance (23) can not be canceled, resulting in slightly lower isolation between these elements. However, in the receive mode the isolation is actually improved by using the pre-amplifier decoupling technique (6). This was realized in the Neurovascular array by phase shifters that compensate for phase delay in the cables between the coil elements and the system pre-amplifiers, such that the low input impedance of the pre-amplifier is actually transferred to the coil input.

Table 3.1. Design parameters of the Neurovascular array.

Coil Name	Head-Vertical	Head-Horizontal	Helmholz-Pair	Butterfly
Element Number	1	2	3	4
1	-22dB	-23dB	-16dB	-21dB
2	-23dB	-19dB	-22dB	-18dB
3	-16dB	-22dB	-24dB	-20dB
4	-21dB	-18dB	-20dB	-21dB

For all elements, the ratio between the unloaded and loaded Q factors is higher than 8, indicating a load-dominant situation.

Simulation Results

Head Birdcage Simulation Results

Field results. All field simulations were performed for main current of 1A in the Birdcage. In this case the current magnitude is 1A in all bar segments.

Simulation results for the head Birdcage coil in the X-Z plane are shown in Figure 3.11. Plots a) and b) are the vertical and horizontal field components, and c) is the total rotating field for circularly polarized excitation.

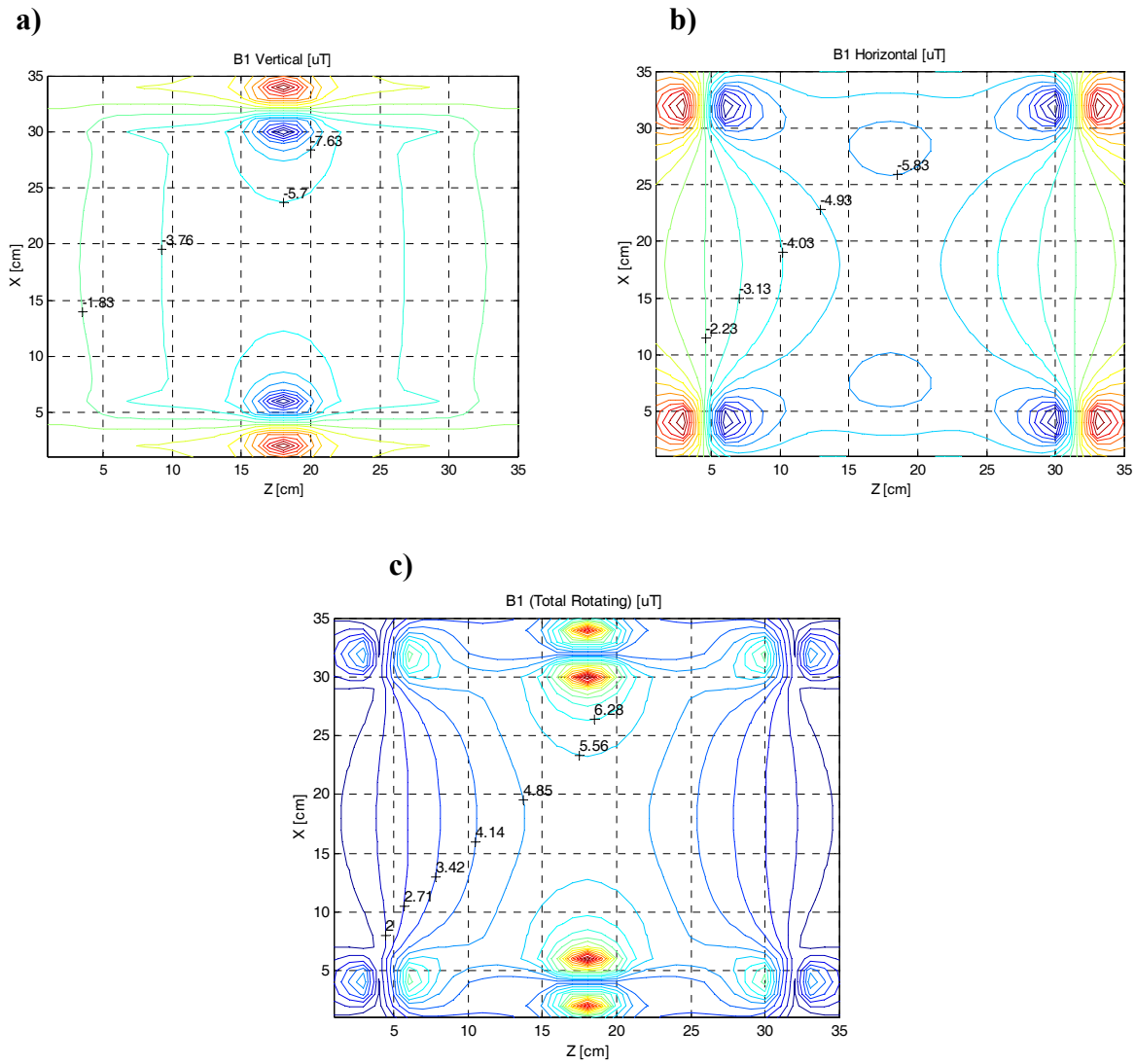

Figure 3.11. Field simulation results for the Birdcage coil in the X-Z plane. a) Vertical field. b) Horizontal field. c) Total rotating field.

Figure 3.12 shows the results in the transverse (X-Y) plane.

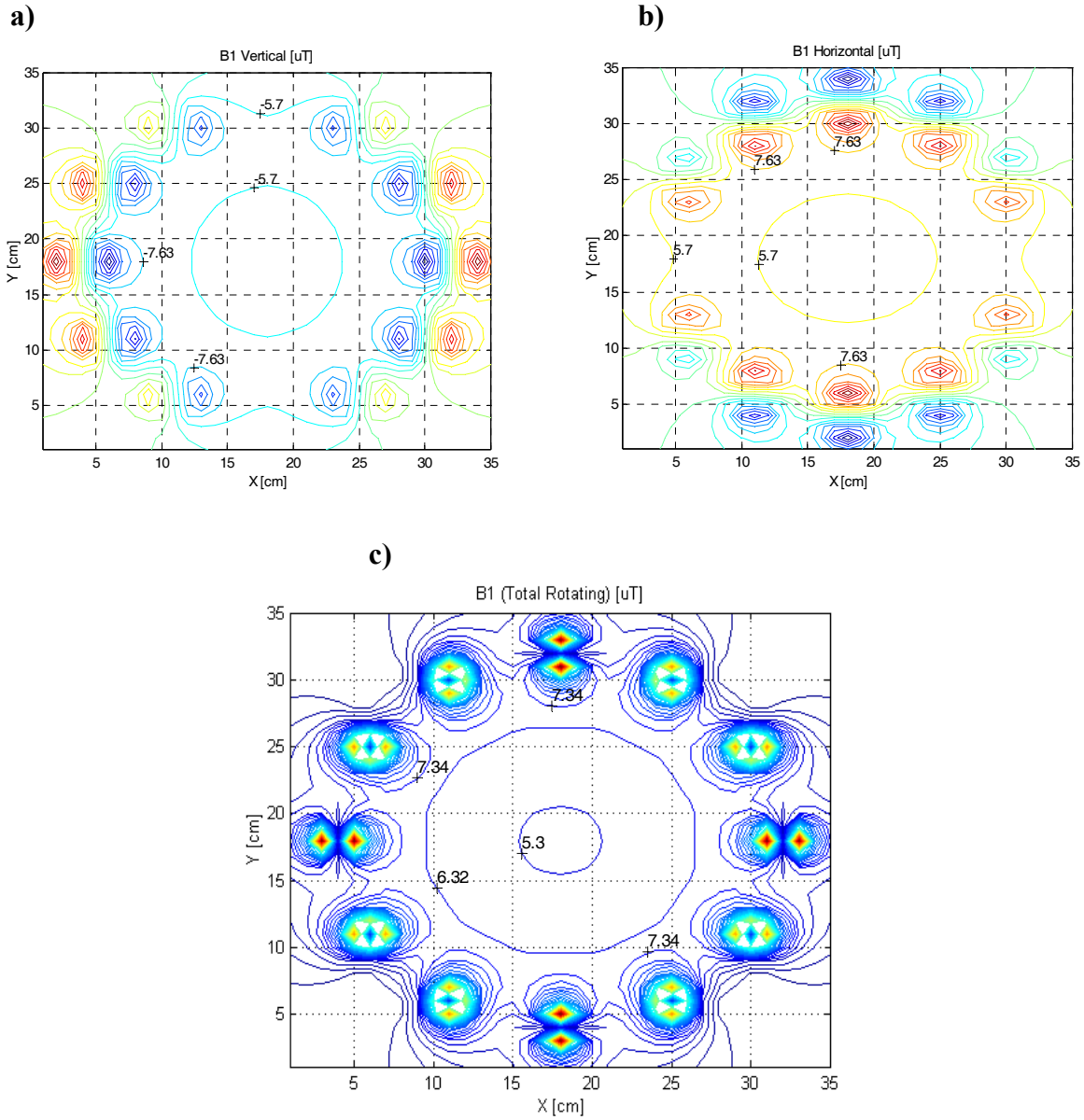

Figure 3.12. Field simulation results for the Birdcage coil in the X-Y plane. a) Vertical field. b) Horizontal field. c) Total rotating field.

SAR results. Local SAR results in the center transverse plane (Z=0) are shown in Figure 3.13 for load diameter of 20cm (4cm form coil conductors—a), and for load diameter of 26cm (1cm form coil conductors—b)

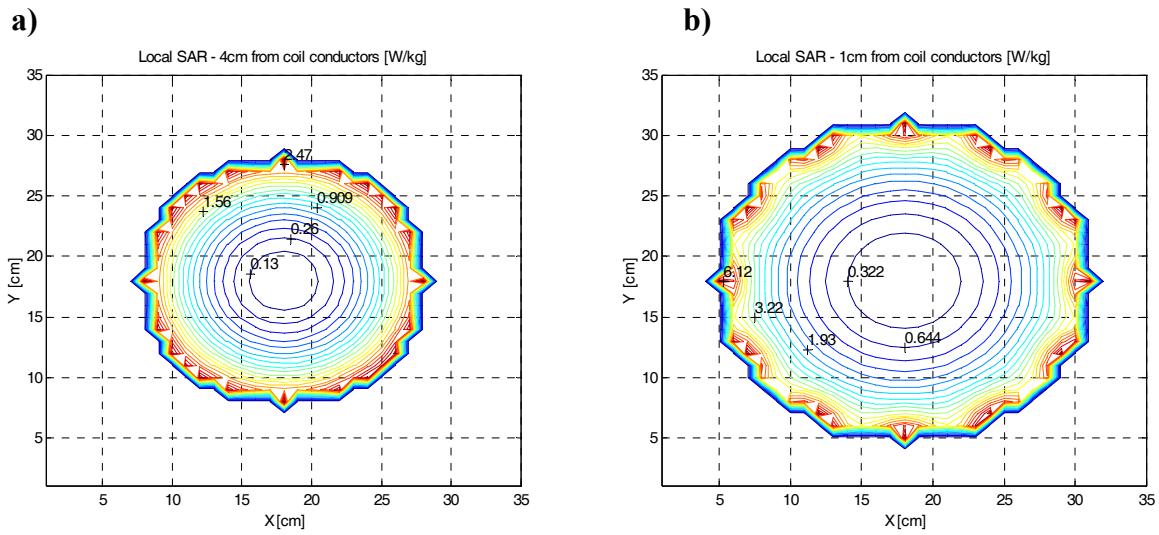

Figure 3.13. Local SAR levels at Z=0. a) For load diameter of 20cm. b) For load diameter of 26cm.

The maximum local SAR is 2.47W/kg and 6.12W/kg respectively for 20cm load and 26cm load. The Average SAR (over the entire cylindrical load) was calculated to be 1.45W/kg for the 20cm load, and 2.43W/kg for the 26cm load.

The local SAR at the transverse plane of the Birdcage end-ring (Z=13.5) is shown in Figure 3.14.

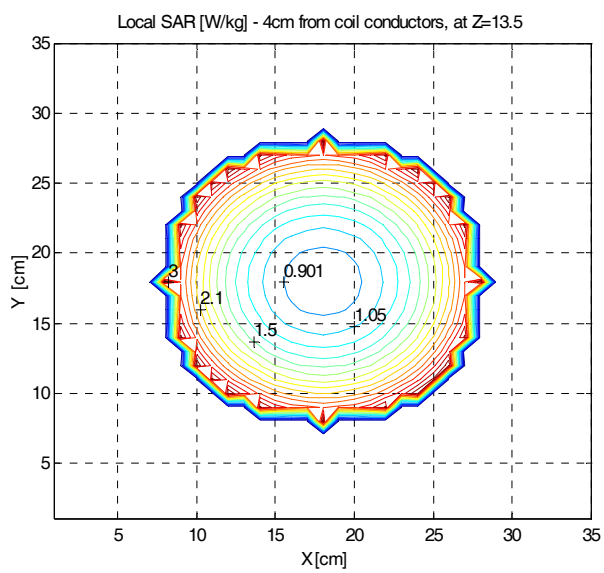

Figure 3.14. Local SAR levels at Z=13.5 for load diameter of 20cm.

It should be noted that these SAR results were computed for current of 1Amp in the Birdcage elements with duty-cycle of 5%. This current level yields a rotating field of approximately 6μT in the center of the coil. However, a typical 180° RF pulse requires higher field, so that the SAR levels need to be scaled accordingly. In additional, typical scan in 3.0T field is performed in lower duty-cycle (2-3% or lower) such that SAR limits are not exceeded.

Neck Helmholtz-Pair Simulation Results

Field results. All field simulations were performed for current of 1Amp in the Helmholtz-Pair coil. Simulation results are shown in the X-Y plane (Figure 3.15a) and in the X-Z plane (Figure 3.15a). Only the vertical field is shown, as this is the only significant component.

a) **b)**

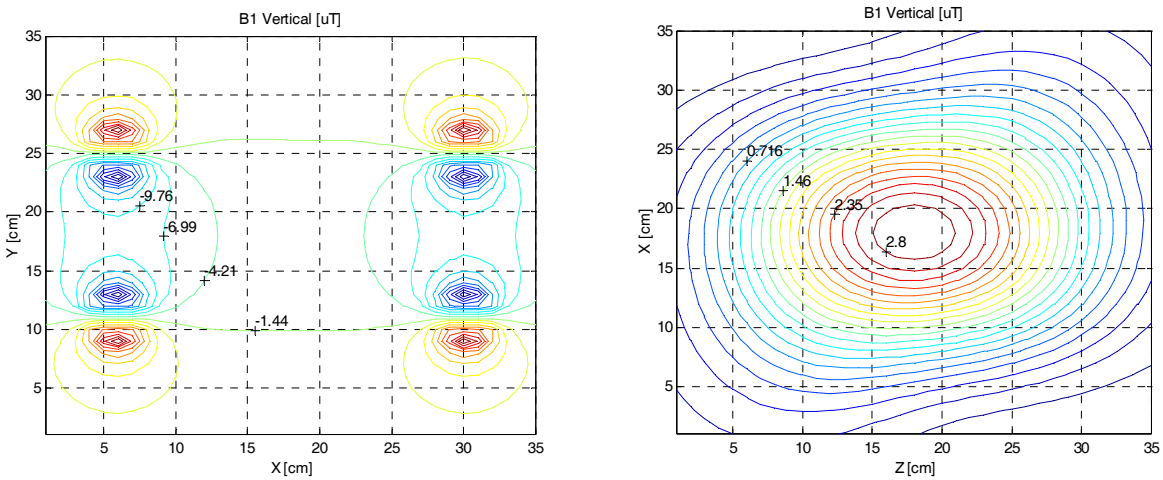

Figure 3.15. Field maps of the Helmholtz-Pair coil. a) In the X-Y plane. b) In the X-Z plane.

SAR results. The average SAR for the two load sizes are 0.21W/kg (20cm load) and 0.38W/kg (26cm load). These values are lower that those obtained for the Birdcage coil. However, it should be noted that for the same unit current, the magnetic field in the

center of the Helmholtz-Pair coil is lower than the Birdcage. In addition, being a linear coil, the Helmholtz-Pair coil requires twice higher power than the quadrature Birdcage in order to obtain the same NMR excitation. With these factors in consideration, the average SAR level for the Helmholtz-Pair is comparable to this of the Birdcage. In addition, since the current in the Helmholtz-Pair is distributed in only 4 longitual conductors, the local SAR is significantly higher than that of the Birdcage.

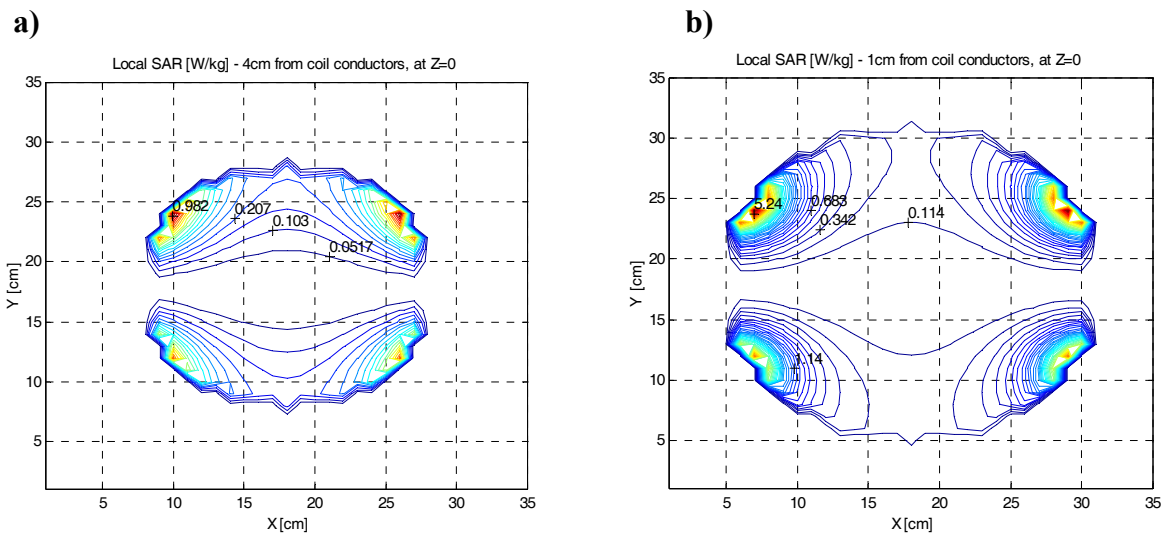

Figure 3.16. Local SAR levels for the Helmholtz-Pair coil at Z=0. a) For load diameter of 20cm b) For load diameter of 26cm.

Phantom Images

Phantom images were acquired at the GE Signa LX 3.0T system at the VA Hospital, Gainesville FL. The protocol is a Fast Spin Echo sequence with the parameters as shown in Table 3.2.

For unloaded SNR assessment, phantom with silicone oil was used. Silicone oil is not conductive so that no eddy currents are developed in the liquid. In addition the relative dielectric constant of Silicone oil is close to 1, so that there are no dielectric resonance effects. These properties allow accurate measurements of unloaded SNR.

Table 3.2. Scan parameters for phantom images.

Parameter	Value
Protocol	FSE
TE	17msec
TR	500msec
ETL (Echo Train Length)	4
Slice Width	3mm
FOV	30x30cm (24x24 for axials)
NEX (Number of Excitations	1
Frequency Encodings	256
Phase Encodings	128

SNR was measured by acquiring the images and saving the raw data for all channels. Then Matlab programs were used to reconstruct using the sum-of-squares algorithm (6). SNR results in coronal (a) and axial (b) center slices are shown in Figure 3.17 for the head channel only. Numbers in the boxes are average SNR results for the pixels within each box.

a) **b)**

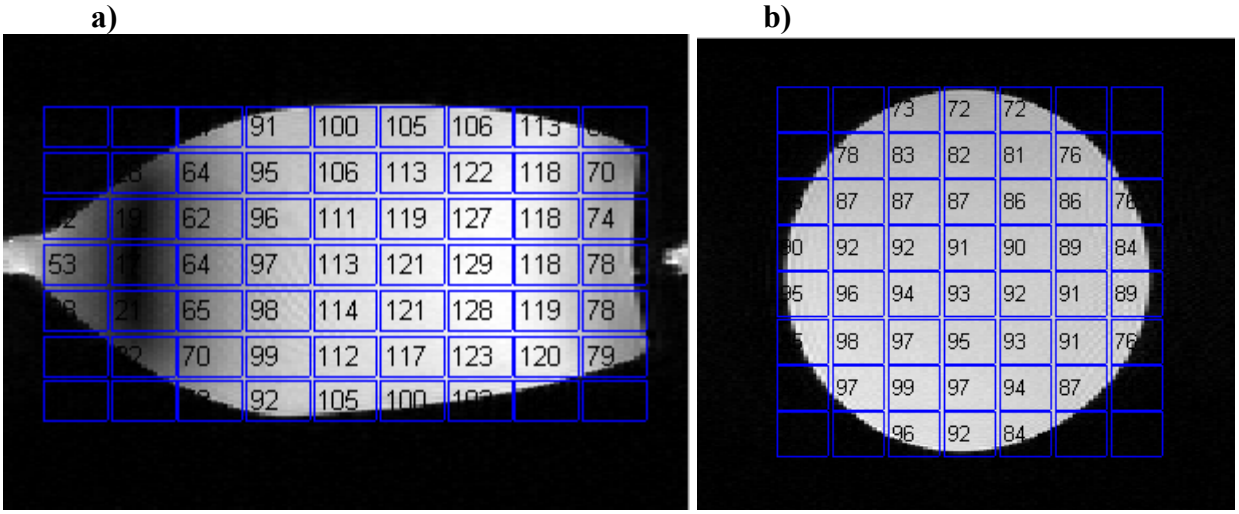

Figure 3.17. Unloaded SNR of the head Birdcage. a) Coronal slice. b) Axial slice.

The distortion in the superior end of the coronal image (the phantom is a cylindrical bottle and is distorted in the right side of the image) is due to gradient non-linearity

within the relatively large FOV. In the MR system, gradient correction algorithm is used so that the images are not distorted. However, this correction is not available in the Matlab reconstruction program. The distortion also causes an artificial increase in the measured SNR in the superior (right side) end of the image. Based on the magnitude of the geometric distortion, this increase in SNR is in the order of 10%.

The measured SNR can be compared to the simulation results that may be obtained by post processing of the B1 calculation as follows: for Spin Echo sequence the SNR of a transmit-receive coil is given by (24)

$$\mathrm{SNR}(\mathbf{r}) = \mathrm{B}_1(\mathbf{r}) \cdot \sin^3\left(\theta(\mathbf{r})\right) \qquad [3.7]$$

where θ(**r**) is the flip angle at point **r**. Simulation results based on Eq. [3.7] are shown for the Z direction (a) and for the X direction (b) in Figure 3.18.

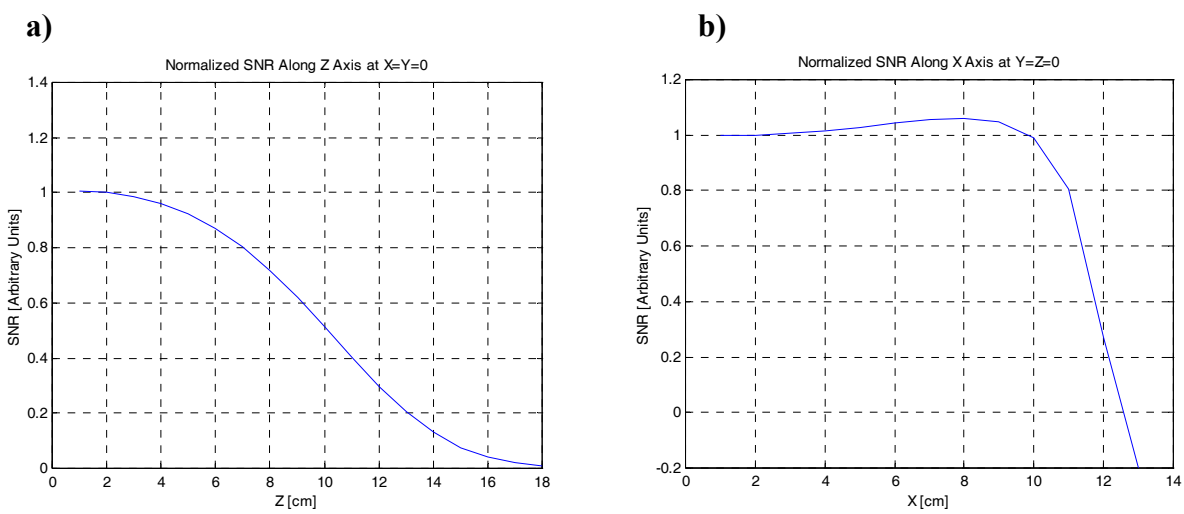

Figure 3.18. Computed SNR for the head Birdcage. a) In the Z direction. b) In the X direction.

From the simulation results in Figure 3.18(a) the drop in SNR is 50% at Z=10cm. This is in good agreement with the measurement in Figure 3.17(a) where SNR drops from 121 in the center box to 64 at approximately 10cm from the center (the FOV is

30cm). In the axial slice, the slight increase in SNR that is predicted by the simulation, was measured only in the left and lower sides of the images, where there is a slight drop in SNR in the right and top sides. These variations are within ±10% and can be explained by imperfect phantom positioning and some non-uniformity in the coil. However, the SNR is relatively uniform within the phantom diameter (16cm), and the drop that is expected at larger diameter, is out of the phantom coverage.

In addition, SNR was compared to that of the GE Head coil (16-pole quadrature Birdcage with 28cm diameter, 30cm length), using the protocol parameters in Table 3.2. The reconstructed images with unloaded SNR measurements are shown in Figure 3.19.

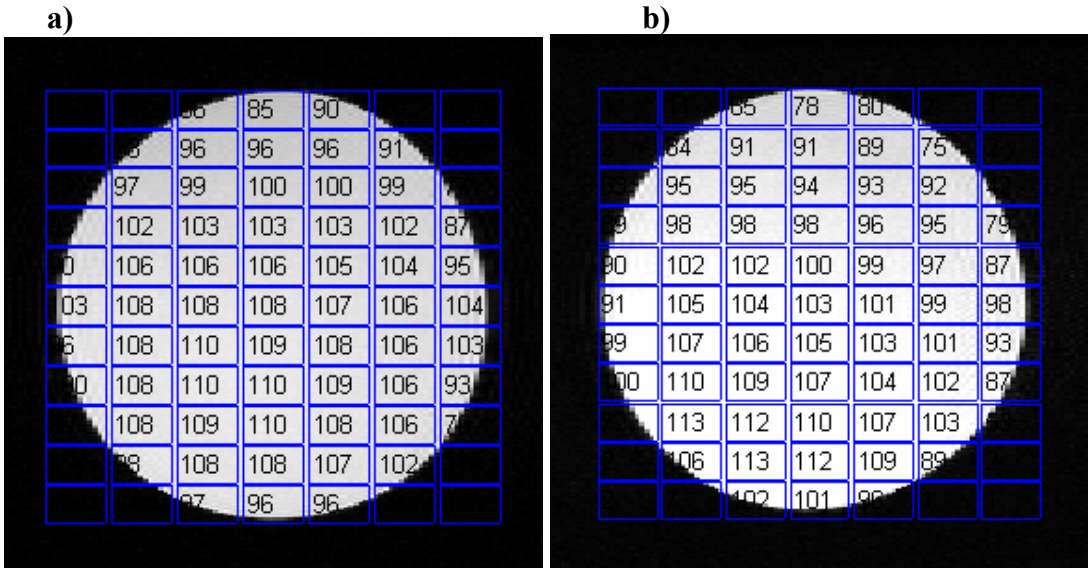

Figure 3.19. Unloaded SNR comparison. a) The GE head coil. b) The Neurovascular array.

Figure 3.20 shows SNR comparison at the head (axial slice) between the Neurovscular array and the GE head coil. The phantom used in this comparison is a distilled water solution doped with NiCl (2 gram/litter) and NaCl (4.5 gram/litter). In this case SNR of the GE head coil is higher by approximately 10%.

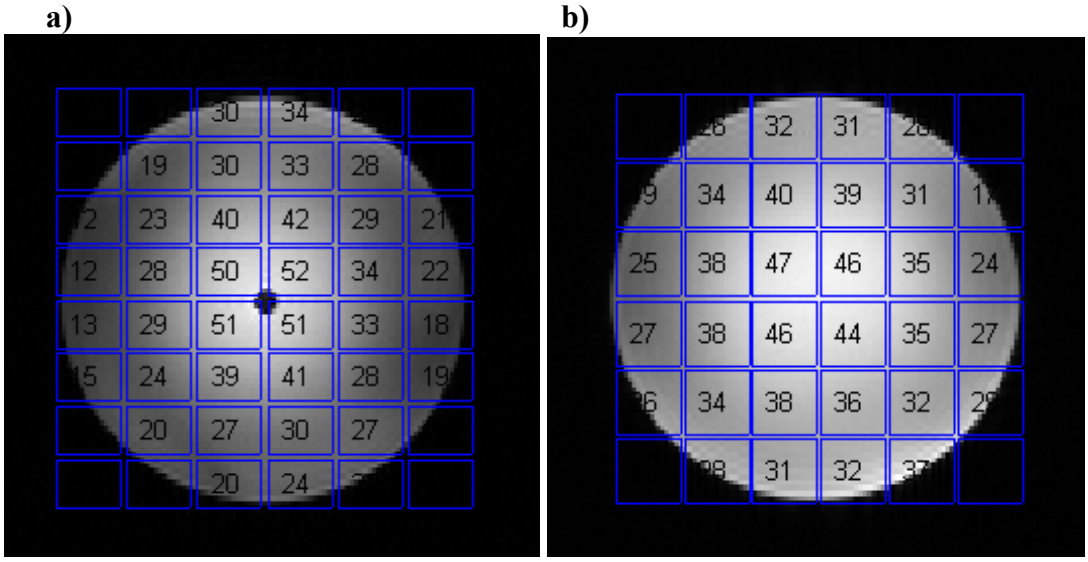

Figure 3. 20. Loaded SNR comparison. a) The GE head coil. b) The Neurovascular array.

The reason for the slight decrease in SNR in the Neurovascular array in the loaded case, is explained by the noise correlation. The noise correlation matrix between the elements of an array can be calculated from the raw data of the individual channel images, based on the background noise pixels. It represents the correlation due to coupling between channels. As described before, this coupling can be as a result of mutual inductance and/or shared resistance. The noise correlation matrices for both unloaded and loaded cases are

$$N_{UNLOADED} = \begin{bmatrix} 1.0000 & 0.0088 & 0.1229 & 0.0900 \\ 0.0088 & 1.0000 & 0.0347 & 0.0134 \\ 0.1229 & 0.0347 & 1.0000 & 0.0569 \\ 0.0900 & 0.0134 & 0.0569 & 1.0000 \end{bmatrix}$$

$$N_{LOADED} = \begin{bmatrix} 1.0000 & 0.0654 & 0.3298 & 0.0494 \\ 0.0654 & 1.0000 & 0.0338 & 0.0364 \\ 0.3298 & 0.0338 & 1.0000 & 0.0087 \\ 0.0494 & 0.0364 & 0.0087 & 1.0000 \end{bmatrix} \qquad [3.8]$$

Most correlation values in the Matrices are close to zero, except for the correlation between channel 1 (vertical mode of the Birdcage) and channel 3 (Helmholtz-Pair). These two elements generate fields in the same direction (not orthogonal to each other). Without the load, good isolation is achieved by conductors overlap, so that the noise correlation is still low ($N_{UNLODED}(1,3) = 0.1229$). However, with the load, additional shared resistance—which can not be cancelled—is involved, such that the noise correlation is much higher: $N_{LODED}(1,3) = 0.3298$. This introduces extra losses to both channels, resulting in approximately 10% SNR decrease in the head area, compared to the GE head coil.

Conclusion

A Neurovascular array with four coil elements was successfully constructed to operate at 127.75MHz. Bench measurement shows that the electrical properties are within the design specifications. All elements were load-dominant indicating that coil losses are insignificant compared to sample losses. In addition coupling between the elements was minimized so that no extra losses were introduced.

Field simulations based on the quasi-static approach, showed that the coil elements can support uniform excitation within large volume and without exceeding SAR limitations. The calculated uniformity in the head region is approximately ±10% in a sphere of 20cm diameter. Local and average SAR were found to be within FDA guidelines for typical scan requirements. In the worse case of 26cm diameter load (only 1cm from coil conductors) the local SAR was found to be 2.5 times higher than the average SAR. This implies that in this case the limitation for scan parameters selection is the local SAR.

Phantom images were acquired for verification of uniformity and for SNR measurements. Results were found to be in good agreement with the simulation prediction. In addition, loaded and unloaded SNR in the head were compared to those obtained with the GE standard head coil. As expected by the similar geometry of the head section in the Neurovascular array and the GE head coil, SNR results of the two coils were comparable.

CHAPTER 4
THE TRANSMIT CIRCUIT AND EXCITATION UNIFORMITY

Introduction

The use of transmit-receive phased arrays requires that a unique power splitter and multiple transmit-receive (T/R) switches be developed just for this purpose. The construction of multiple T/R switches is fairly straightforward and is well known in the field of high frequency MRI coils. However, the design of the required power splitter is not obvious, as the performance of the power splitter—when connected to the coil—are somewhat different from the performance with the standard 50Ω termination. This is due to the non-perfect match of the coil with different loads as well as non-perfect isolation between the coil elements.

Another aspect that affects the splitter design is the influence of coil coupling on the transmit field uniformity. As discussed before, coil coupling (due to mutual inductance) is minimized by the geometric design (coil overlapping and orthogonality). However, in a multi-coil system, some coil coupling between the array elements still exists, and the shared resistance can not be eliminated. During receive mode, this coupling is usually reduced by the low impedance pre-amplifier, but in transmit mode it tends to change the designed field uniformity. This problem needs to be solved by adjusting the power splitter, such that optimal homogeneity is achieved with the presence of coil coupling.

A general block diagram of the transmit power splitter and transmit-receive switches is shown below:

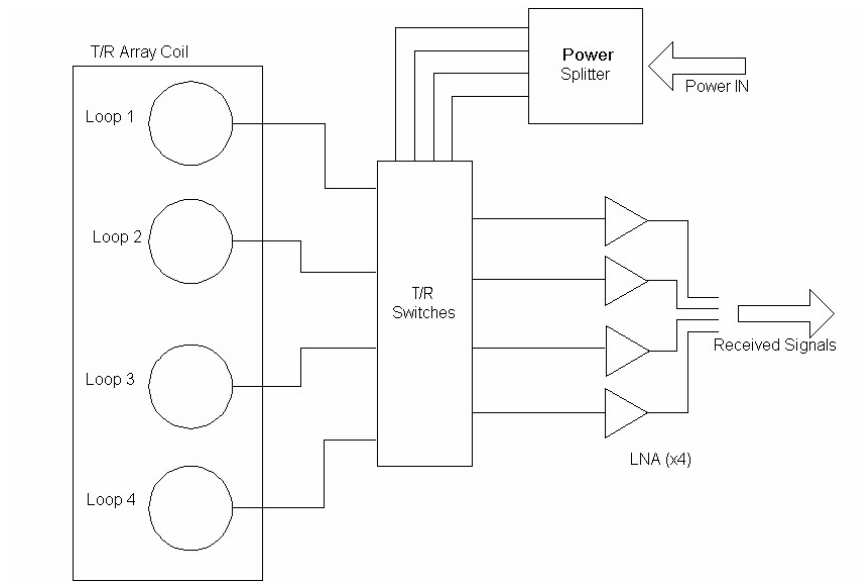

Figure 4.1. Block diagram of the transmit circuit.

Theory

Power Splitter Design

Any N-port circuit can be described by its Scattering Matrix (S-parameters)—a NxN matrix where S_{ii} is the mismatch loss (reflection) in port i, and S_{ij} is the insertion loss (transmission) between port j and i (25).

For a lossless N-port system, power conservation implies that

$$\sum_{m=1}^{N} \left| S_{mj} \right|^2 = 1 \qquad [4.1]$$

for every row or column j.

A standard power splitter is a four-port RF circuit that can be described as follows:

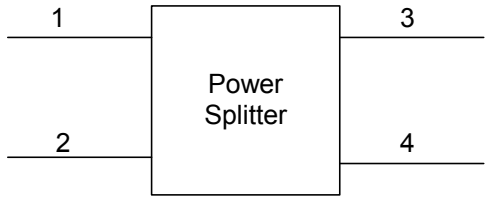

Figure 4.2. Representation of 4-port system.

If port 1 is used for power input, then the split power is at port 3 and 4, and port 2 is the "isolated port", where no power is expected at this port. For an ideal symmetric and lossless 2-way power splitter, where 90° phase difference is required between ports 3 and 4, the S-parameters matrix is

$$S = \begin{bmatrix} 0 & 0 & -iA & B \\ 0 & 0 & B & -iA \\ -iA & B & 0 & 0 \\ B & -iA & 0 & 0 \end{bmatrix} \qquad [4.2]$$

where A and B are scalar constants, that – for power conservation – must satisfy

$$A^2 + B^2 = 1 \qquad [4.3]$$

The ratio between the constants A and B defines the nature of the power splitter. A simple and very useful realization of a 3dB (equal) power splitter is the well known quadrature hybrid, that can be constructed with either λ/8, 50Ω transmission line segments, or lumped elements, as shown in Figure 4.3.

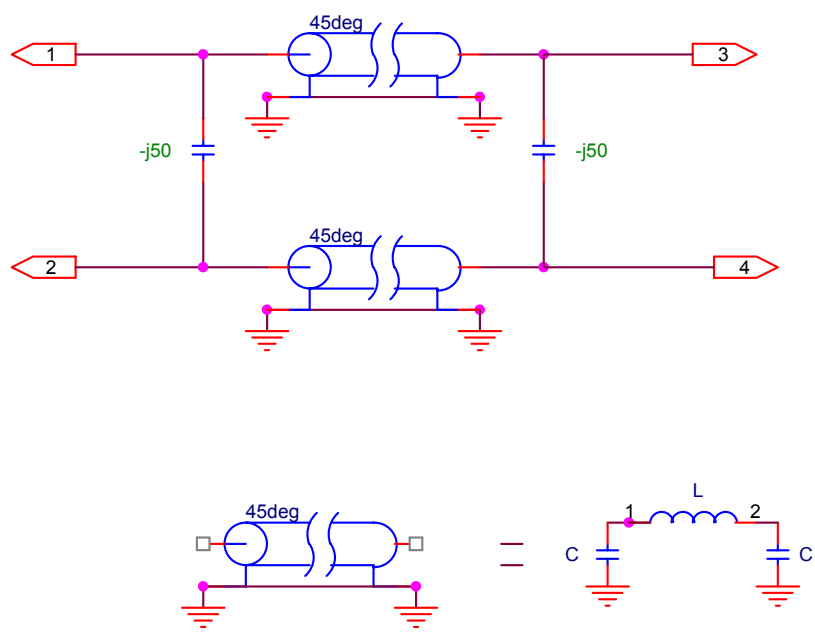

Figure 4.3. Quadrature hybrid with either λ/8 transmission lines, or lumped elements.

The S-parameters representation for this circuit is

$$S = \begin{bmatrix} 0 & 0 & -i\frac{1}{\sqrt{2}} & \frac{1}{\sqrt{2}} \\ 0 & 0 & & \\ -i\frac{1}{\sqrt{2}} & \frac{1}{\sqrt{2}} & 0 & 0 \\ \frac{1}{\sqrt{2}} & -i\frac{1}{\sqrt{2}} & 0 & 0 \end{bmatrix} \qquad [4.4]$$

However, trying to modify this design by only altering the –j50Ω capacitor, so that different power split is obtained, often causes mismatch at all ports and poor isolation. Therefore a generalize approach needs to be taken when a non-equal power splitter is required.

Such general power splitter is shown in Figure 4.4.

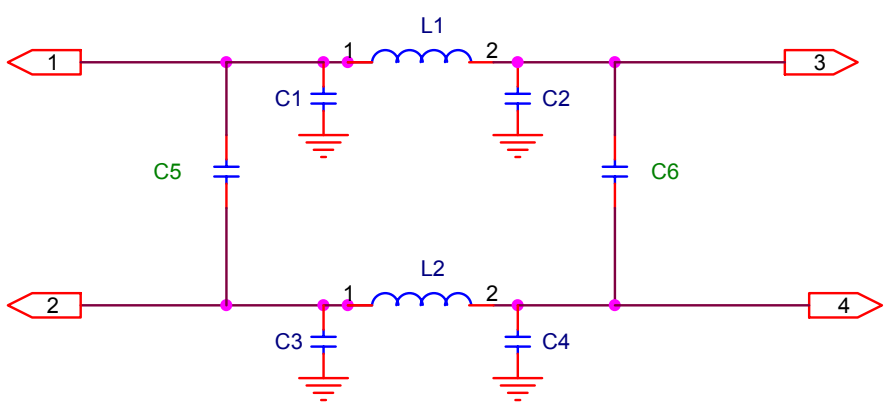

Figure 4.4. Generalized power splitter.

Starting with the general scattering matrix of Eq. [4.2], and by applying symmetry conditions for the even and odd modes, and the condition of Eq. [4.3], the following equations were developed:

$$
\begin{aligned}
Z_{L_{1,2}} &= i \cdot Z_0 \cdot A & \Rightarrow \quad L_{1,2} &= \frac{Z_0 \cdot A}{\omega} \\
Z_{C_{1-4}} &= -i \cdot Z_0 \cdot \left(\frac{A}{1-B}\right) & \Rightarrow \quad C_{1-4} &= \left[\omega \cdot Z_0 \left(\frac{A}{1-B}\right)\right]^{-1} \\
Z_{C_{5,6}} &= -i \cdot Z_0 \cdot \left(\frac{A}{B}\right) & \Rightarrow \quad C_{5,6} &= \left[\omega \cdot Z_0 \left(\frac{A}{B}\right)\right]^{-1}
\end{aligned}
\qquad [4.5]
$$

where ω is the operating frequency, and A and B define the power split.

For N dB power split, A and B are given by

$$
\begin{aligned}
B &= 10^{-\left(N/20\right)} \\
A &= \sqrt{1-B^2}
\end{aligned}
\qquad [4.6]
$$

Field Simulation of the Array

In order to obtain uniform excitation when transmitting with the array, a simulation model of the array was used to determine the required power split.

The array elements that are used for the transmission are the head Birdcage and the neck Helmholtz-Pair. These elements were simulated together, using the following structure:

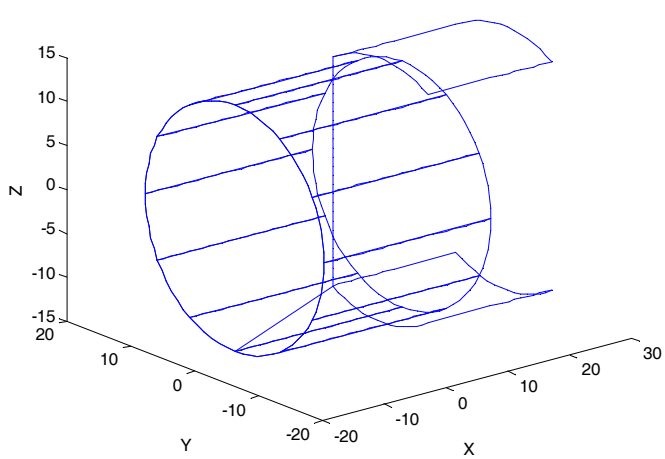

Figure 4.5. Birdcage and Helmholtz-Pair for excitation uniformity simulation.

Using the simulation technique described in details in Chapter 3, the magnetic field at the center, along the Z-axis was calculated. The main current in the Birdcage was set to be 1, and the current in the Helmholtz-Pair coil was altered to optimize the field uniformity. Results for different Helmholtz-Pair currents are shown in Figure 4.6.

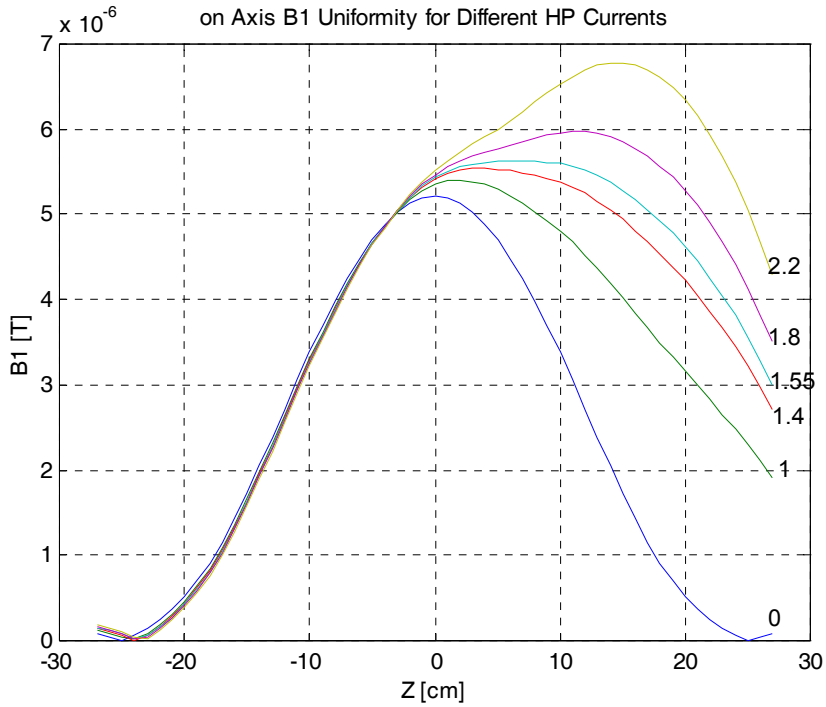

Figure 4.6. Simulation results for optimum excitation uniformity.

From Figure 4.6 we learn that optimum uniformity is obtained for current ratio of 1.55. Therefore, the required power splitter is such that A/B=1.55. In order to satisfy Eq. 4.3, we then obtain: A=0.84, and B=0.54, which yields a 5.3dB power splitter.

Methods

Power Splitter

Design

According to Eq.4.5 and 4.6, and with the splitter specifications developed above, the following component values were calculated (referred to Figure 4.4):

$$L_{1,2} = \frac{Z_0 \cdot A}{\omega} = 52.2\text{nH}$$
$$C_{1-4} = \left[\omega \cdot Z_0 \left(\frac{A}{1-B}\right)\right]^{-1} = 13.5\text{pF} \qquad [4.7]$$
$$C_{5,6} = \left[\omega \cdot Z_0 \left(\frac{A}{B}\right)\right]^{-1} = 16.1\text{pF}$$

Circuit simulation

The circuit described in Figure 4.4, with the component values calculated in Eq. 4.7 was simulated using ARRL—RF circuits simulation program (26). Results are shown in Figure 4.7.

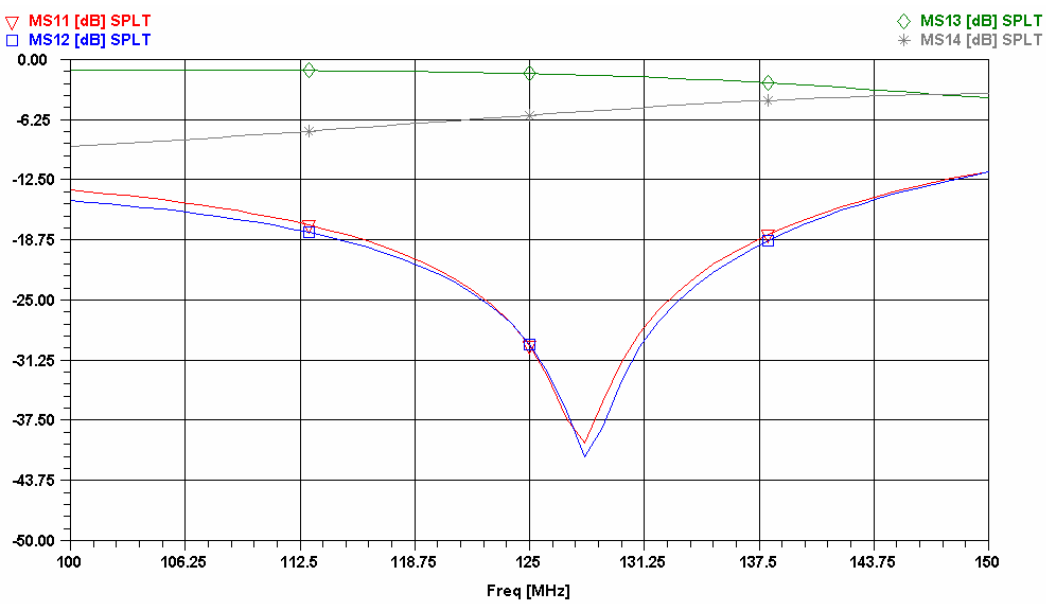

Figure 4.7. Simulation results for 5.3dB power splitter.

At the frequency of interest (127.75MHz), the power splitter parameters are:

Table 4.1. Simulation results at 127.75MHz.

Freq [MHz]	MS_{11} [dB]	MS_{12} [dB]	MS_{13} [dB]	MS_{14} [dB]	PS_{13} [°]	PS_{14} [°]
127.75	-39.98	-40.41	-1.61	-5.43	-89.5	-0.3

The simulation results verify the design method and shows that the design goals were achieved. Also, the phase angle between ports 3 and 4 is 90° as required.

T/R Switches

The use of transmit-receive phased arrays implies that the coil elements are used for both power transmission and signal reception. Therefore, a transmit-receive (T/R) switch needs to be used in order to isolate the receiver from the coil during transmit phase, and to prevent signal loss into the transmitter during receive phase. The construction of T/R switches is fairly straightforward and is well known in the field of high frequency MRI coils. Such a T/R switch is shown in Figure 4.8.

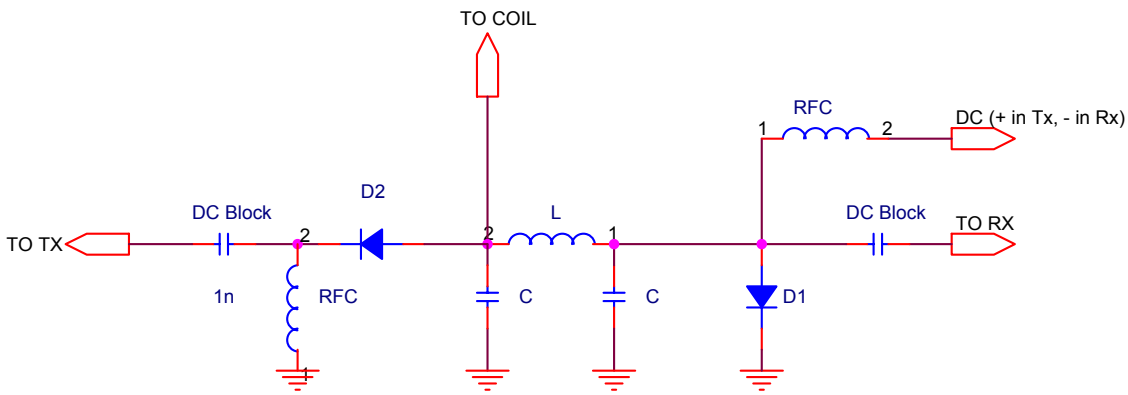

Figure 4.8. Schematic diagram of a T/R switch.

The capacitors C and inductor L are designed to create a 90° phase shifter in the frequency of interest. In transmit mode, positive voltage is provided, so that both PIN diodes are forward biased and present short impedance at high frequency. Therefore the coil element is connected to the transmitter via D_2, while D_1 and the phase shifter form high impedance towards the receiver. In receive mode, negative DC voltage is provided, so that the PIN diodes are reversed biased. In this case the coil is disconnected from the transmitter, and connected through the 90° phase shifter to the receiver. Typical

parameters of such T/R switch are insertion loss of 0.2-0.3 dB and isolation of approximately 40dB.

In the Neurovascular array, the above circuit was used with 4.7μH inductors for RFC, 1nF capacitors for DC blocking and the PIN diodes are of type MA4P1250 (M/COM, USA). L and C are of 50Ω reactance at 127.75MHz (62nH, and 24pF respectively).

The Transmit Circuit-Coil System

The block diagram of the entire Neurovascular array system is shown in Figure 4.9. It should be noted that the fourth coil element (receive-only butterfly) is not shown. The phase shifter at the receiver connection are designed to compensate for phase delay in the cables and circuitry between the coil elements and the system preamplifiers, so that pre-amplifier decoupling is obtained in receive mode. The quadrature-hybrid (QH) in Figure 4.9. is the standard 3dB power splitter.

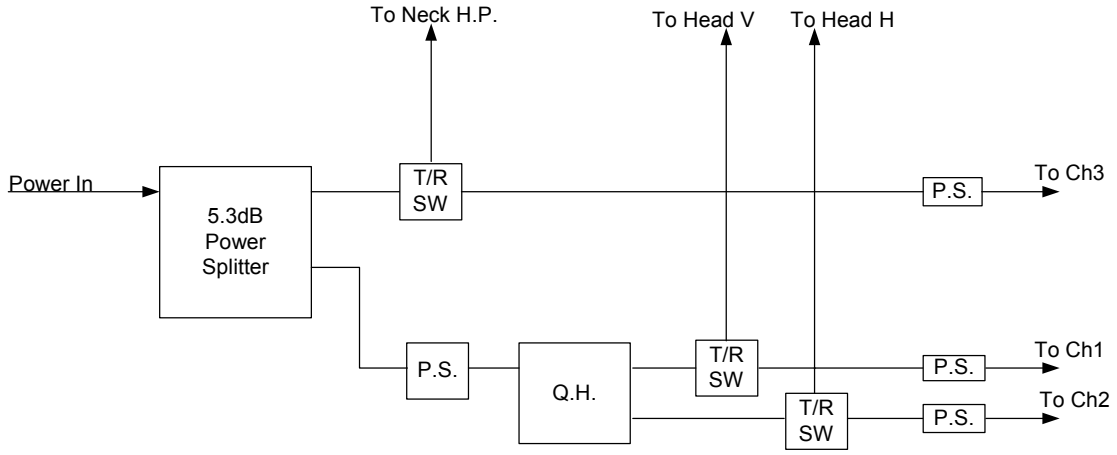

Figure 4.9. Block diagram of the entire transmit circuit-coil system.

Results and Discussion

Power Splitter

The entire power splitter of Figure 4.9. was constructed on several PC boards with coaxial cable connections between them. Component values are as follows (refer to the schematic in Figure 4.4):

Table 4.2. Components values in actual power splitter.

Power Splitter	Component	Theoretic	Actual
Main	$L_{1,2}$	52.2nH	52nH [1]
	C_{1-4}	13.5pF	12pF [2]
	C_{5-6}	16.1pF	16pF
QH	$L_{1,2}$	44.0nH	44nH [1]
	C_{1-4}	10.3pF	10pF
	C_{5-6}	24.9pF	24pF

[1] Inductors were measured and adjusted, so good accuracy was achieved.
[2] Lower capacitor was required to compensate for parasitic stray capacitance.

Measurements at the power splitter outputs (coil connection ports) are summarized in Table 4.3.

Table 4.3. Power splitter measurements.

Measurement Point	Magnitude	Phase
Port 1 – BC vertical connection	-1.9dB	-117°
Port 2 – BC vertical connection	-8.6dB	-127°
Port 3 – BC horizontal connection	-8.6dB	-31°
Reflection at All Ports	<-23dB	-
Isolation Between All Ports	<-20dB	-

Considering that the attenuation of each port of the QH is approximately 3.3dB, the power levels at the main power splitter ports are –1.9dB and –5.3dB. This is in good agreement with both the design parameters and the simulation results. Also, from Table 4.3, the phase relation between the two head ports is 96°, which is required to obtain circularly polarized field.

Field Measurements

With the transmit circuit connected to the Neurovascular array, the system was placed in a bore simulator, to provide the shielding conditions as in the MR system. Then the magnetic field was measured in different locations and orientations, using a small field probe (Emco, USA). Results are summarized in Table 4.4.

Table 4.4. Field measurements.

Measurement Point	Magnitude [dB]	Phase
Center of Birdcage, horizontal	-42.1	+47°
Center of Birdcage, vertical	-42.4	-37°
Center of Helmholtz-Pair, vertical	-36.5	-42°

This shows that the phase relations between field components is correct in order to support circular polarization. Also, components of same orientation are in phase, to prevent points of field cancellation. In addition, it should be noted that although the field of the Helmholtz-Pair is higher than that of the Birdcage, it is still not high enough. Based on the field uniformity simulation (requires +3.8dB), and the fact that the circularly polarized field needs to be 3dB higher than linear field, the Helmholtz-Pair field needs to be approximately 6.8dB than this of the Birdcage. This result was confirmed also by the initial field mapping, and the main power splitter was adjusted to enhance the Helmholts-Pair field, by changing $C_{5,6}$ to 18pF.

B_1 Field Mapping

B1 maps where reconstructed using the algorithm in (24), which is briefly explained here: When acquiring two Spin Echo images with flip angles θ1 and θ2, the ratio between the signals is

$$r = \frac{\sin^3 \theta_1}{\sin^3 \theta_2} \qquad [4.8]$$

With flip angles chosen such that $\theta_2 = 2\theta_1$ the signal ratio is reduced to

$$r = \frac{1}{[2 \cdot \cos\theta_1]^3} \qquad [4.9]$$

Substituting $\theta_1 = \gamma B_1 t$ and solving for B_1 the field map can be calculated by

$$B_1 \propto \cos^{-1}\left[\left(\frac{1}{8 \cdot r}\right)^{1/3}\right] \qquad [4.10]$$

B_1 maps where reconstructed by acquiring 2 consecutive Spin Echo (SE) images with flip angles of 60° and 120° respectively, and with Matlab program that computes Eq. 4.10 from the raw data. Due to the difficulty in obtaining a phantom that correctly represents tissue parameters in all aspects of resistive loading, capacitive loading, dielectric effects and RF eddy currents, volunteer images where used to asses B_1 uniformity. Results in all 3 planes are shown in Figure 4.10. Numbers in the boxes indicate actual flip angle, where nominal 90° is assumed at the center 9-pixels of each image. The drop in flip angle at the superior and inferior ends of the sagittal and coronal slices is mainly due to dielectric effect. This is significantly minimized when a smaller (and more clinically useful) FOV is selected.

a) **b)**

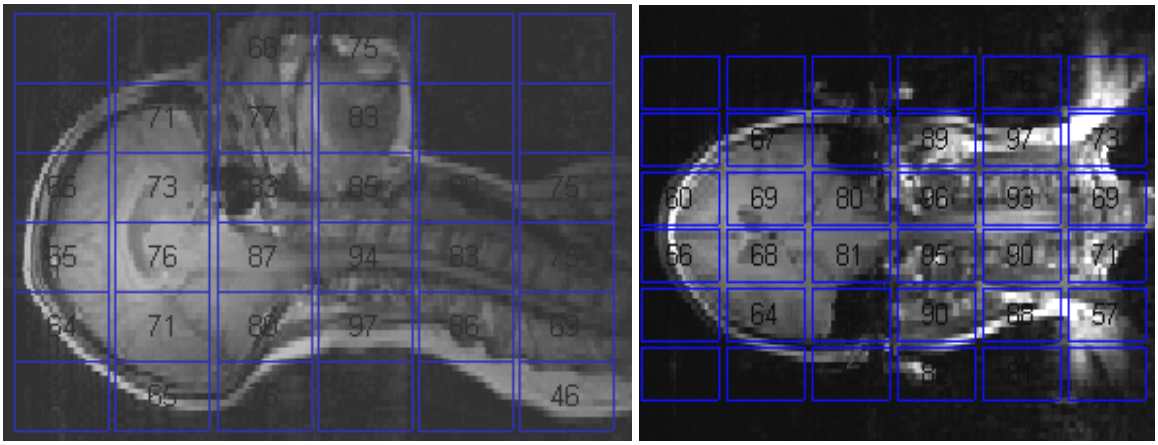

c)

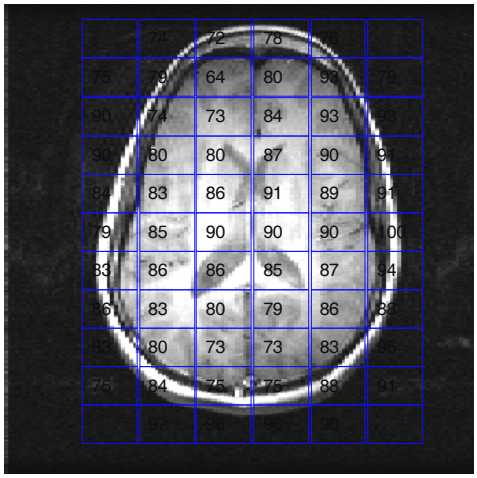

Figure 4.10. Flip angle maps. a) In sagittal slice. b) In coronal slice. c) In axial slice.

Conclusion

Field simulation methods were used to determine and optimize the required power split for the Neurovascular array. The optimum ratio between current in the Helmholtz-Pair coil and the Birdcage (main current) was found to be 1.55, which yield a 5.3dB power splitter. Such power splitter was designed using a generalized design method for non-equal power split. The power splitter was first simulated and then constructed. Both

simulation results and measured parameters were in excellent agreement with the design specifications.

The power splitter and other transmit circuitry were integrated into the Neurovascular array and B_1 maps were acquired in order to verify the uniformity of the excitation field. According to initial results and bench measurements, the power splitter was slightly adjusted, such that the transmit field uniformity was optimized.

The final results of transmit flip angle maps demonstrate that good uniformity was obtained in all directions and over the entire coil coverage, without any significant voids or hot spots. The required RF power is approximately twice that of the GE head coil. The required peak power for 180° excitation pulse was approximately 2kw for 75kg female and slightly higher for a 30 years old, 80kg athletic male. This higher power was expected due to the larger coverage of the array, and the linear excitation at the neck Helmholtz-Pair. Nevertheless, this level is still much lower than the reported power required for a whole body RF coil (up to 25kw (9)), so that the average SAR level for neurovascular application is minimized with the Neurovascular T/R array.

CHAPTER 5
THE ANATOMICAL AREA AND CLINICAL IMAGES

Introduction—Anatomy

Cervical Spine

The cervical spine is made up of the first seven vertebrae in the spine. It starts just below the skull and ends at the top of the thoracic spine. The cervical spine has a backward "C" shape (lordotic curve) and is much more mobile than either of the thoracic or lumbar regions of the spine.

The first two vertebral bodies in the cervical spine are called the atlas and the axis. The atlas is named such, because this is the vertebral body that supports the weight of you head. The atlas and axis vertebrae in the cervical spine differ from all other vertebrae because they are designed primarily for rotation. The atlas has a thick forward (anterior) arch and a thin back (posterior) arch, with two prominent masses.

The axis sits underneath the atlas and has a bony knob called the odontoid process that sticks up through the hole in the atlas. It is this mechanism that allows the head to turn from side to side. There are special ligaments between these two vertebrae to allow for rotation between these two bones.

The cervical vertebral bodies are smaller than those in the other spinal segments and increase in size downward. Foramina are large openings in the bone that allow the passage of arteries, nerve roots and the spinal cord itself. Intervertebral discs are located between the vertebral bodies. The outer layers of the discs are comprised of layers of

fibrous tissue and is called the annulus fibrosus. The inner zone, or the nucleus pulposus, is made up of springy and pulpy matter (27).

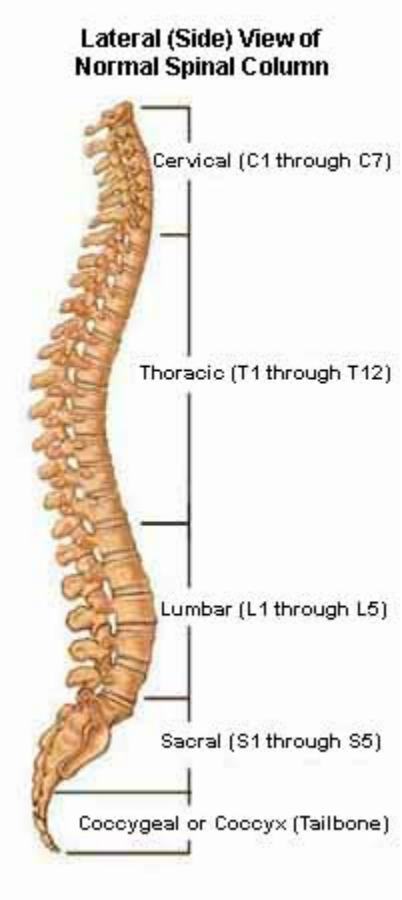

Figure 5.1. The spinal column.

Carotid Artery

The carotid arteries are the four principal arteries of the neck and head. They have two specialized regions: the carotid sinus, which monitors the blood pressure, and the carotid body, which monitors the oxygen content in the blood and helps regulate breathing. The internal carotid arteries enter the skull to supply the brain and eyes. At the base of the brain, the two internal carotids and the basilar artery join to form a ring of blood vessels called the "circle of Willis." The external carotid arteries have several branches, which supply the tissues of the face, scalp, mouth and jaws.

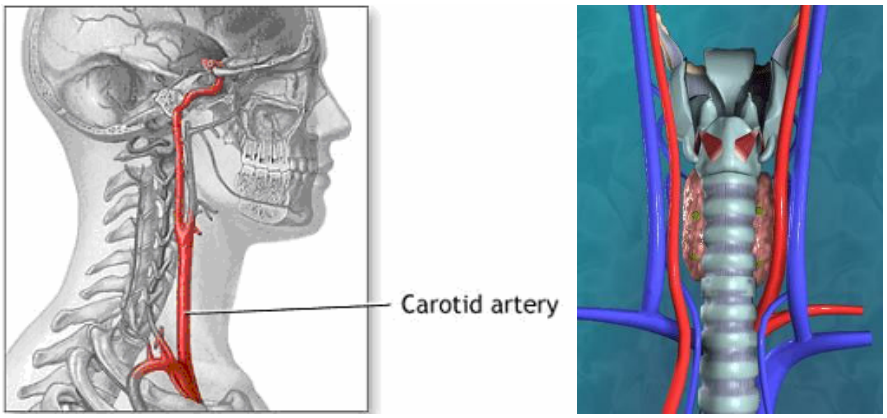

Figure 5.2. The carotid artery.

Circle of Willis

At the base of the brain, the carotid and vertebrobasilar arteries form a circle of communicating arteries known as the circle of Willis.

From this circle other arteries—the anterior cerebral artery (ACA), the middle cerebral artery (MCA), and the posterior cerebral artery (PCA)—arise and travel to all parts of the brain.

Because the carotid and vertebrobasilar arteries form a circle, if one of the main arteries is occluded, the distal smaller arteries that it supplies can receive blood from the other arteries (collateral circulation).

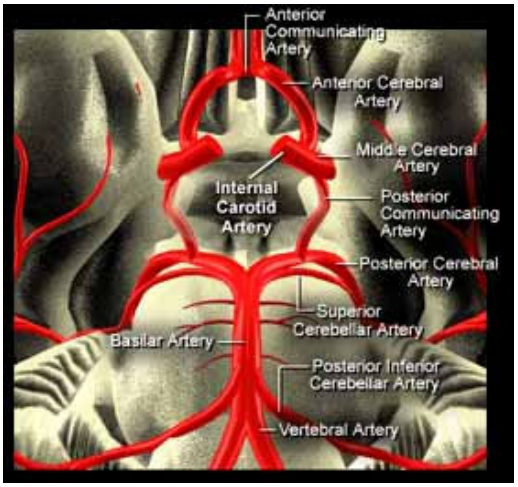

Figure 5.3. Circle of Willis.

Clinical Imaging with the Neurovascular Array

Clinical imaging with the Neurovascular Array was performed at the GE Signa 3.0T MR System at the VA Hospital, Gainesville FL. Imaging was performed with two volunteers under IRB, as the Neurovascular array is not FDA cleared and the system is FDA approved for head imaging only. A general problem in performing the clinical imaging was the lack of appropriate and specific protocols for this coil. This is due to the reason that clinical work in this site is done in head imaging only. Therefore, for carotids imaging (MR angiography), sequences that are normally used for head MRA were used, with the minimal necessary modifications. For cervical spine imaging, simple FSE and GRE protocols were used, just to demonstrate coil capability.

Another obstacle in the clinical work was power limitations of the system. As discussed in chapters 4, power requirements of the Neurovascular array are higher than that of the GE head coil, which is the standard coil in the system. When using the Neurovascular array, this fact causes 2 problems: first, the average power limit of the system is exceeded, and the peak power needed is higher than the available power. The former can be avoided by simply reducing the number of slice. However the later prevents the use of certain higher power sequences. This power limitation is soon to be solved, as the system will be upgraded, so that future work with the Neurovascular array would not be restricted by power limitations.

Cervical Spine Images

The general purpose of cervical spine imaging is to show the anatomical structure of the cervical vertebras (C1 through C7), the discs structures and the spinal cord in the neck region. Usually both T_1 and T_2 weighting are required, and slightly larger coverage (S-I) is preferred to show the first thorastic vertebras and the brain stem as well.

Images were acquired with 39 years old female as follows:

- T_2 weighted fast spin echo (FSE-xlc/90) with TE=87msec, TR=3200msec, 31.2KHz, 20cm FOV, 3mm sagittal slice, 3 excitations, 384x224 matrix (3:47min).

Figure 5.4. T_2 weighted sagittal fast spin echo image of the cervical spine.

Image shows good penetration to the cervical vertebras, good coverage and uniformity in the S-I direction, such that the brain stem and T1 are clearly shown.

- T_1 weighted spin echo (SE) with TE=8msec, TR=500msec, 15.6KHz, 20cm FOV, 3mm sagittal slice, 3 excitations, 256x256 matrix (6:30min).

Figure 5.5. T_1 weighted sagittal spin echo image of the cervical spine.

Again, good coverage and uniformity are demonstrated. The distortion in the lower jaw is due to magnetic tooth filling.

- T_1 weighted gradient spin echo (GRE/90) with TE=3.6msec, TR=500msec, 15.6KHz, 16cm FOV, 3mm axial slice, 2 excitations, 256x256 matrix (4:20min).

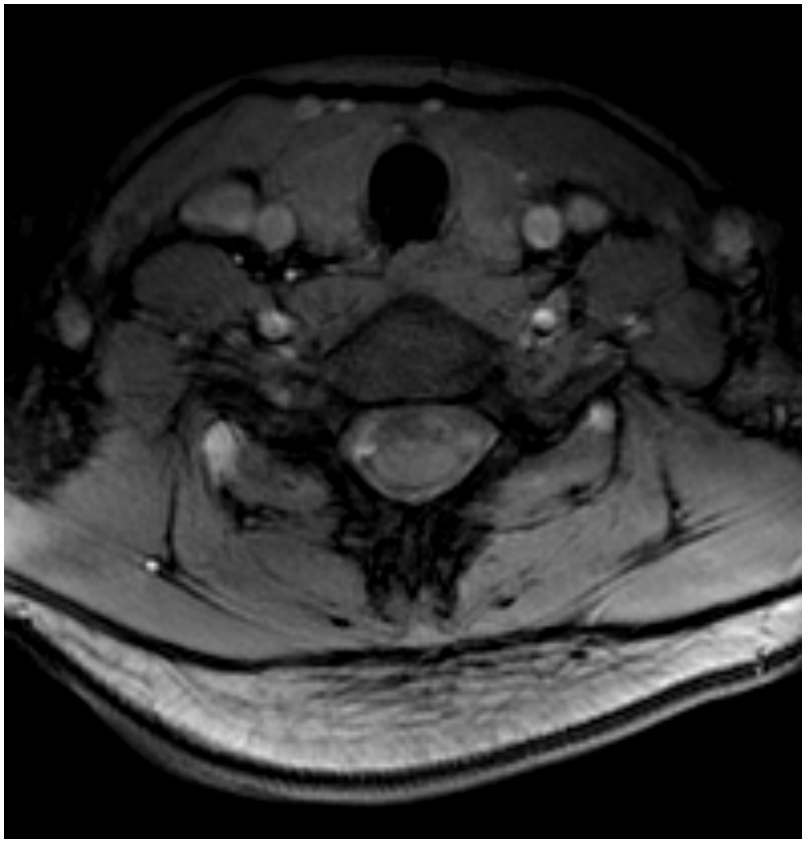

Figure 5.6. T_1 weighted axial gradient echo image at C4.

This image shows good penetration and good uniformity in the A-P direction. Both the vertebra and the spinal cord are clearly seen.

Carotids and Circle of Willis Images

These images were acquired using different techniques of MR angiography (MRA) (28,29), to show blood flow in the carotid arteries up to the circle of Willis. As stated before lack of specific protocols impaired the ability to obtain images of great clinical quality, but the images show the capabilities of the Neurovascular array w/o contrast enhancement.

- Time-of-flight (TOF/SPGR/50) with TE=4.7msec, TR=23msec, 16.0KHz, 26x20cm FOV, 1.5mm coronal slice, 1 excitation, 256x128 matrix (1:48min).

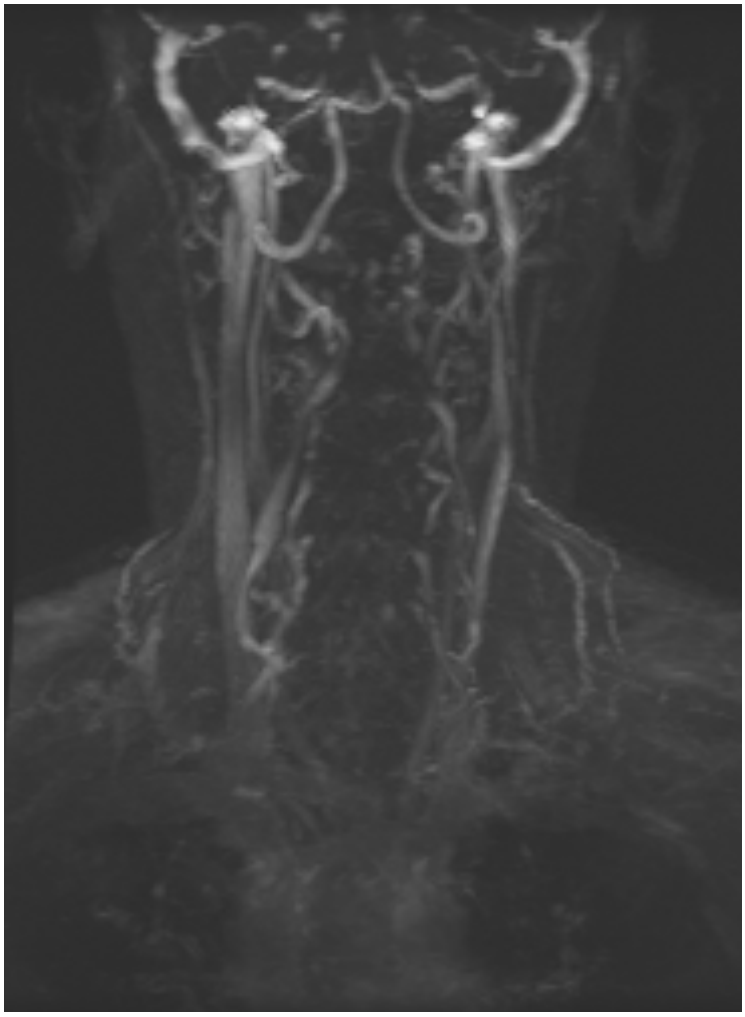

Figure 5.7. Coronal MRA of the carotids.

This image shows the left and right carotid arteries from the aortic arch to the circle of Willis. Although the image is blared in the arch area (probably due to non-optimized protocol parameters), it shows the coverage capability of the coil.

- 3D Time-of-flight (TOF/SPGR/50) with TE=6.9msec, TR=35msec, 31.2KHz, 26x20cm FOV, 1.6mm sagittal slice, 1 excitation, 512x256 matrix (5:26min).

Figure 5.8. Sagittal high resolution 3-D TOF of the left carotid artery.

This image shows the high-resolution capability of the Neurovascular array, were high SNR is obtained with small slice thickness and large matrix (512x256).

Conclusion

The clinical imaging with the Neurovascular array demonstrated the high performance capability of the device – high SNR, good uniformity and large coverage. A good imaging system is presented to the known problem of power availability and SAR levels in high field MR imaging. The Neurovascular array presented in this work addresses this problem by excitation of much smaller volume – only this required for the imaging. The local nature of transmitting with this coil results in much lower power than a whole body coil. As shown before this is an advantage in patient safety aspects, but also in economic concerns.

Other advantages of the Transmit/Receive Neurovascular Array over the use of a whole body transmit coil and a local receive-only array, are related to imaging techniques

and image artifacts. One of the artifacts in imaging with a receive only coil, arises from the fact that the whole body coil excites not only the tissue in the imaging area, but also outside this region. This fact, together with selecting a field of view that is larger than the imaged object, causes the problem known as wrap around (aliasing), where signal from outside the field of view is folded into the image. A typical solution to the problem in single dimension is by selecting the phase encoding direction properly. This creates an undesired constrain in scan parameter selection. However, the use of smaller transmit coil which does not excite tissue outside the interesting field of view eliminates the artifact completely.

Other applications that would prefer local tissue excitation are spectroscopy, magnetization transfer methods and chemical suppression. These methods are based on the different resonance frequency of different materials (for example water and fat). However, due to magnet imperfect uniformity, the larger the excitation volume is, the broader each frequency peak becomes, so that it is difficult to distinguish between the different resonances. A smaller transmit coil would allow narrow peak for each resonance frequency and would allow better definition of the different materials.

The last imaging techniques were not demonstrated in this work. However, the inherent high SNR and good uniformity of the Neurovascular array ensure good results and high image quality with these methods as well.

APPENDIX A
MATLAB PROGRAMS

N-Bars Birdcage Coil

```
%            BC-N.M

%            BIRDCAGE - N BARS
%            =================
% This program calculates and draws an N-bars birdcage.
% The outputs are 3 vectors: x, y, z, which contain the coordinates of
% the structure segments, and a vector I which contains the current of
each element
% ____________________________________________________________________

clear all;
close all;

  %     parameters
   %    ----------

   prompt = {'Enter the Birdcage Diameter [cm] :','Enter the Birdcage
Length [cm] :','Enter Number of Bars :'};
   title = 'Input for Birdcage Simulation';
   def = {'28' , '27' , '12'};
   lineNo = 1;
   dim = inputdlg(prompt,title,lineNo,def);

        r = (str2num(char(dim(1)))) / 2;  % Radius of Birdcage
        H = str2num(char(dim(2)));       % Length of Birdcage
        N = str2num(char(dim(3)));        % No. of bars

 h1 = H/2;

% In is relative currents in the n-th birdcage mesh.

x = [];
y = [];
z = [];
I = [];

main_cur = 1;
start_point = [r 0 (-h1)];

for n=0:N-1

   [xx yy zz II] = bc_mesh(start_point,r,h1,n,N,main_cur);
   x = [x xx];
   y = [y yy];
   z = [z zz];
```

```
   I = [I II];
start_point = [x(end) y(end) z(end)]

end;

m = length(x);

 rot

plot3(x,y,z)  ,grid
xlabel( 'X');
ylabel( 'Y');
zlabel( 'Z');
rotate3d;

%q_bio_savart
bio_savart_2D_E_3D;

q_graphics;
```

Helmholts-Pair Coil

```
%            SADDLE.M

% This program calculates and draws a saddle (Helmholts-Pair).
% The outputs are 3 vectors: x, y, z, which contain the coordinates of
% the structure segments, and a vector I which contains the current of
each element
% ____________________________________________________________________
clear all;
close all;

%       parameters
%       ----------

   prompt = {'Enter the cylinder Diameter [cm] ','Enter the saddle
length [cm]','Enter the Z offset [cm]','Enter the saddle angle [deg]'};
   title = 'Input for Saddle Simulation';
   def = {'28','20','30','60'};
   lineNo = 1;
   dim = inputdlg(prompt,title,lineNo,def);


R = (str2num(char(dim(1)))) / 2;    % Radius of cylinder
H = (str2num(char(dim(2))));        % Length of saddle
offset = (str2num(char(dim(3))));        % Offset in Z-direction
alpha_deg = (str2num(char(dim(4))));    % Angle of saddle

alpha = alpha_deg * pi/180;
start_point = [R*cos(alpha/2) R*sin(alpha/2) -H/2] % start point of 1st
loop
N = 360/alpha_deg;

x=[];
y=[];
z=[];
I=[];

[x, y, z, I] = saddle_mesh(start_point,R,H/2,-alpha_deg,1);

start_point2 = start_point - [2*R*cos(alpha/2) 0 0]

[xx yy zz II] = lin2(start_point,start_point2,0);  %line between the 2
loops with 0 current

x=[x xx];
y=[y yy];
z=[z zz];
I=[I II];

[xx, yy, zz, II] = saddle_mesh(start_point2,R,H/2,alpha_deg,1);

x=[x xx];
y=[y yy];
z=[z zz] + offset;
I=[I II];
```

```
%plot3(x(1:end-5),y(1:end-5),z)
plot3(x,y,z,'r-')
xlabel('X');
ylabel('Y');
zlabel('Z');

m = length(x);
rot;

plot3(x,y,z)
xlabel('X');
ylabel('Y');
zlabel('Z');


%q_bio_savart;
bio_savart_2D_E_3D;
q_graphics;
```

Field Calculation

```
%          BIO_SAVART_2D_E_3D.M

% Simulation of the magnetic field (B1 - DC approximation) in the X-Y
plane, and of
% the electric field (Quazistatic approximation).
% The source is an arbitrary current contour which should be defined by
4 vectors:
% X, Y, Z - which contain the geomentric structure points.
% I - contains the current magnitude of each element.
% (all 4 vectors must have identical length)
% B1 is calculated in 2D X-Y plane.
% E-field is calculated in 3D volume.


title = 'Input for Measurment Plane Definition';
prompt = {'Enter the X center point [cm] :' , 'Enter the Y center point
[cm] :' , 'Enter the FOV [cm] (must be odd) :' , 'Enter the Z location
[cm] :'};
def = {'0' , '0' , '35' , '0'};
lineNo = 1;
plane = inputdlg(prompt,title,lineNo,def);

x_center = str2num(char(plane(1)));  % X center point
y_center = str2num(char(plane(2)));  % Y center point
FOV = str2num(char(plane(3)));       % FOV in cm
z_pos = str2num(char(plane(4)));     % Z position

title = 'Input for Load Definition';
prompt = {'Enter the load diameter [cm] :' , 'Enter the load length
[cm] :' , 'Enter the z-offset [cm] :', 'Enter the Frequency [MHz] :'};
def = {'20' , '30' , '0 ', '127.75'};
lineNo = 1;
plane = inputdlg(prompt,title,lineNo,def);

load_diameter = str2num(char(plane(1)));
load_length = str2num(char(plane(2)));
z_offset = str2num(char(plane(3)));
freq = 1e6 * str2num(char(plane(4)));

x_fov = FOV;
y_fov = FOV;
z_fov = FOV;

sz = length(x);

Bx = zeros(FOV);
By = zeros(FOV);
Bz = zeros(FOV);
dBx = zeros(FOV);
dBy = zeros(FOV);
dBz = zeros(FOV);

Ex = zeros(x_fov,y_fov,z_fov);
Ey = zeros(x_fov,y_fov,z_fov);
```

```
Ez = zeros(x_fov,y_fov,z_fov);
dEx = zeros(x_fov,y_fov,z_fov);
dEy = zeros(x_fov,y_fov,z_fov);
dEz = zeros(x_fov,y_fov,z_fov);

%Init Constants:
%----------------
%freq = 128e6;        % Larmor frequency in MHz
omega = 2*pi*freq;    % Larmor frequency in MRadians/sec
Mu = 4*pi*1e-7;       % [Henry/m]
sigma = 0.9;          % Maximum conductivity in Siemens/meter @64MHz
Io = 1;               % RF current amplitude [Amp]
DC = 0.05;            % Duty Cycle for power calculation


x_test = ones(FOV,1) * [-(x_fov-1)/2 : 1 : (x_fov-1)/2];
x_test_3D = repmat(x_test,[1 1 FOV]);% for 3D,copy into page
dimension(3) load_length times

y_test = [-(y_fov-1)/2 : 1 : (y_fov-1)/2]' * ones(1,FOV);
y_test_3D = repmat(y_test,[1 1 FOV]);     %copy into page dimension
load_length times

z_test = [-(z_fov-1)/2 : 1 : (z_fov-1)/2]' * ones(1,FOV);
z_test_3D1 = repmat(z_test,[1 1 FOV]);    %copy into page dimension
load_length times
z_test_3D = permute(z_test_3D1,[3 2 1]);           %switch x and z
indices to get z_test_3D

% calculate unit vector along the current line:
%-----------------------------------------------
dx = x(1:end-1) - x(2:end);
dx(sz) = dx(sz-1);
dy = y(1:end-1) - y(2:end);
dy(sz) = dy(sz-1);
dz = z(1:end-1) - z(2:end);
dz(sz) = dz(sz-1);

%**********************************
% Bio - Savart Loop
%**********************************

for j = 1:sz
  j
  % calculate distance matrices:
  %-----------------------------
  x_dist_3D = x_test_3D - x(j);
  y_dist_3D = y_test_3D - y(j);
  z_dist_3D = z_test_3D - z(j);

  x_dist = x_test - x(j);
  y_dist = y_test - y(j);
  z_dist = z_test - z(j);

  % s_to_t - Source-to-Test point distance
  s_to_t = ((x_dist).^2 + (y_dist).^2 + (z_dist).^2) .^ 0.5;
```

```
  s_to_t_3D = ((x_dist_3D).^2 + (y_dist_3D).^2 + (z_dist_3D).^2) .^
0.5;

    [x_ind y_ind] = find(s_to_t<2);   % to prevent singularity
  for index=1:length(x_ind)
     s_to_t(x_ind(index), y_ind(index)) = 2;
  end;

  %ind = find(s_to_t<2);   % to prevent singularity
  %s_to_t(ind) = 2;

  ind3 = find(s_to_t_3D<2);   % to prevent singularity
  s_to_t_3D(ind3) = 2;

  % calculate the cross-product [dx dy dz] X [dist_x dist_y dist_y]
  % when dist_x/y/z are matrices.
  % That means that the product is 3 matrices which describes the 3
components
  % of the magnetic field.

  crsp_x = (dy(j).*z_dist) - (dz(j).*y_dist);
  crsp_y = (dx(j).*z_dist) - (dz(j).*x_dist);
  crsp_z = (dx(j).*y_dist) - (dy(j).*x_dist);

  dBx = 100 * (Mu*Io*I(j)/(4*pi)) .* crsp_x ./ ((s_to_t).^3);    %in
[T]
  dBy = 100 * (Mu*Io*I(j)/(4*pi)) .* crsp_y ./ ((s_to_t).^3);    %in
[T]
  dBz = 100 * (Mu*Io*I(j)/(4*pi)) .* crsp_z ./ ((s_to_t).^3);    %in
[T]

  dEx = (-omega) * (Mu*Io*I(j)/(4*pi)) .* dx(j) ./ ((s_to_t_3D));
%in [v/m]
  dEy = (-omega) * (Mu*Io*I(j)/(4*pi)) .* dy(j) ./ ((s_to_t_3D));
%in [v/m]
  dEz = (-omega) * (Mu*Io*I(j)/(4*pi)) .* dz(j) ./ ((s_to_t_3D));
%in [v/m]

  % Note: The factor 100 in the B-field calculation is due to the fact
that the
  %       x,y,z dimentions are in cm while Mu is in [H/m].
  %       In the E-field, the [cm] is canceled in "dx/s_to_t" so no
factor is needed and the result is in [v/m].

  Bx = Bx + dBx;
  By = By + dBy;
  Bz = Bz + dBz;

  Ex = Ex + dEx;
  Ey = Ey + dEy;
  Ez = Ez + dEz;

end;

sample = zeros(x_fov,y_fov,z_fov);
test = (x_test_3D).^2 + (y_test_3D).^2;
true = find(test <= (load_diameter/2)^2);
```

```
sample(true) = 1;
zz = fix((z_fov - load_length)/2);
zz1 = zz - z_offset;
zz2 = zz + z_offset;
sample(:,:,1:zz1) = 0;
sample(:,:,(z_fov-zz2):end) = 0;

losses = sample .* (abs(Ex).^2 + abs(Ey).^2 + abs(Ez).^2);

rr = sum(sum(sum(losses)));

%noise = sqrt((1+1/Qr) .* rr)  % Qr is the unloaded Q to loaded Q ratio
noise = sqrt(rr);
dv = 1e-6;  % dx=dy=dz=1cm --> dv=(1e-2)^3
Peak_power = sigma/2 * rr * dv % peak power deposited in the load
DC
Ave_power = Peak_power * DC
load_volume = pi * (load_diameter/2)^2 * load_length   %in [cubic cm]
load_weight = load_volume   % in [grams], assuming load density = 1
gr/cm3
Ave_SAR = Ave_power / (load_weight/1000)  % in [watt/kg]
max_local_SAR = (sigma/2) * max(max(max(losses))) * DC * 1e-3  % in
[watt/kg]
% since the element size is 1 cubic cm, the max element is max local
SAR
```

LIST OF REFERENCES

1. C.P. Slichter, Principles of Magnetic Resonance. Springer-Verlag, Berlin, Germany, 2nd ed. (1978).

2. F. Bloch, W.W. Hansen, M. Packard, Nuclear Induction. *Phys. Rev.* **69**, 127 (1946).

3. T.C. Farrar, E.D. Becker, Pulse and Fourier Transform NMR. Academic Press, Inc., Toronto (1971).

4. E. L. Hahn, Spin Echoes. *Phys. Rev.* **80**, 580-594 (1950).

5. J. Pauly, P. LeRoux, D. Nishimura, A. Macovski, Parameter Relations for the Shinnar-Le Roux Selective Excitation Pulse Design Algorithm. *IEEE Trans. Med. Imaging* **10**, 53 (1991).

6. P.B. Roemer, W.A. Edelstein, C.E. Hayes, S.P. Souza, O.M. Mueller, The NMR Phased Array. *Mag. Res. Med.* **16**, 192-225 (1990).

7. K.P. Pruessman, M. Weiger, M.B. Scheidegger, P. Boesiger, SENSE: Sensitivity Encoding for Fast MRI. *Mag. Res. Med,* **42**, 952-962 (1999).

8. D.K. Sodickson, W.J. Manning, Simultaneous Acquisition of Spatial Harmonics (SMASH): Ultra Fast Imaging with Radiofrequency Coil Arrays. *Mag. Res. Med.* **38**, 591-603 (1997).

9. J.W. Hugg, M.A. Bernstein, S. Stokar, C. Lin, D. Rosenfeld, J.P.Felmlee, A. Montag, J. Huston III, B. Assif, H.G. Reynolds, Routine Clinical Head MRI at 3.0T with Optimized RF Power Management. *Proc. ISMRM*, 1349 (2001).

10. S. Roberts, A. Freeman, P. Murphy, R. Gauss, M. Burl, High Definition Whole Body Imaging at 3 Tesla. *Proc. ISMRM*, 2013 (2001).

11. R.D. Watkins, J.F. Schenck, K.W. Rohling, J. Piel, D. Rosenfeld, D. Kelley, R. Lenkinski, H. Kressel and A. Montag, Whole Body RF Coil for 3 Tesla MRI System. *Proc. ISMRM*, 1123 (2001).

12. S.D. Wolff, R.S. Balaban, Magnetization Transfer Contrast (MTC) and Tissue Water Proton Relaxation Invivo. *Magn. Reson. Med*. **10**, 135-144 (1989).

13. D.I. Hoult, R.E. Richards, The Signal-to-Noise Ratio of the Nuclear Magnetic Resonance Experiment. *J. Magn. Reson.* **24**, 71-85 (1976).

14. J. Jin, Electromagnetic Analysis and Design in Magnetic Resonance Imaging. CRC Press, New York (1998).

15. D.I. Hoult, P.C. Lauterbur, The Sensitivity of the Zeugmatographic Experiment Involving Human Samples. *J. Magn. Reson.* **34**, 425-433 (1979).

16. J. Murphy-Boesch, and A.P. Koretsky, An in Vivo NMR Probe Circuit for Improved Sensitivity. *J. Magn. Reson*, **54**, 526-532 (1983).

17. D.M. Peterson, G.R. Duensing, and J.R. Fitzsimmons, MRI Basics and Coil Design Principles. *RF Design*, 56-64 (January 1997)

18. C.E. Hayes, W.A. Edelstein, J.F. Schenck, O.M. Mueller, M. Eash, An Effective Highly Homogeneous Radiofrequency Coil. *J. Magn. Reson*, **63**, 622-628 (1985).

19. J. Troop, The Theory of the Bird-Cage Resonator. *J. Magn. Reson*, **82**, 51-62 (1989).

20. W.T. Sobol, Dedicated Coils in Magnetic Resonance Imaging. *Reviews of Magn. Reson. Med*. **1**, 181-224 (1986).

21. Birdcage Builder Version 1.0 Penn State University (1988)

22. O.P. Gandhi, J.Y. Chen, Absorption and Distribution Patterns of RF Fields*, Annals New York Academy of Science,* 131-143.

23. C.E. Hayes, J.S. Tsuruda, C.M. Mathis, Temporal Lobes: Surface MR Coil Phased Array Imaging. *Radiology,* **189**, 918-920 (1993).

24. E.K. Insko, L. Bolinger, Mapping of the Radiofrequency Field, *J. Magn. Reson*, **103**, 82-85 (1993).

25. H.A. Atwater, Introduction to Microwave Theory. McGraw-Hill, New York, USA (1962).

26. ARRL Radio Designer Version 1.5, Compact Software Inc., Paterson NJ (1993).

27. F.H. Netter, The CIBA Collection of Medical Illustrations, (Vol 1: Nervous System, Part 1: Anatomy and Physiology). Icon Learning Systems, Los Angeles, CA (1983).

28. C.L. Dumoulin, Phase-Contrast Magnetic Resonance Angiography, *Neuroimaging Clinics of North America*, Vol. 2, **4**, 657-676 (1992).

29. J.E. Potchen, Magnetic Resonance Angiography, Concepts and Applications Mosby, St Louis, Missouri (1993).

BIOGRAPHICAL SKETCH

Shmuel Gotshal was born in Petach-Tikva, Israel, on November 23, 1962, and lived in Petach-Tikva until 1982. At that time he graduated high school and joined the Israel Defense Force (IDF) where he served for four years. In 1986 the author started to attend the Tel Aviv University and graduated with a Bachelor of Science in electrical engineering in 1990. He also married his wife Noa in June 1886. In 1991, he accepted a position with the Israeli company Elscint as a research and development engineer in the MRI division, and was promoted to the position of RF Team Leader in 1996. In 1996 he also started to attend the Technion—Israel Institute of Technology, pursuing a master's degree in biomedical engineering. In May 1999, he moved with his family to Gainesville, FL, where he took his current position as the Manager of Electrical Engineering at MRI Devices Corporation—an industry leader that develops and manufactures RF coils for MRI. He also continued his studies towards a master's degree at the University of Florida.

In addition to design and construction of MRI coils, the author has been active in publishing papers relating to MRI coil design in relevant conferences.